Science of the Total Environment 962 (2025) 178357

Contents lists available at ScienceDirect

Science of the Total Environment

journal homepage: www.elsevier.com/locate/scitotenv

Aerosol transport and associated boundary layer thermodynamics under contrasting synoptic conditions over a semiarid site

Sandip Pal [a,*], Nicholas E. Prince [a,b], Michael Anand [a,c], Matthew Hamel [a,d]

[a] Department of Geosciences, Atmospheric Science Division, Texas Tech University, Lubbock, TX, USA
[b] Department of Meteorology and Atmospheric Science, The Pennsylvania State University, University Park, PA, USA
[c] National Weather Service Office, Albuquerque, NM, USA
[d] National Wind Institute, Texas Tech University, Lubbock, TX, USA

HIGHLIGHTS

- Boundary layer aerosols under synoptically active and benign weather conditions
- Advection-dominated features in aerosol mixing processes
- Impact of fronts and lifting on aerosol horizontal and vertical transport processes
- Changes in aerosol features via dryline, airmass exchange and wind shift over dryland

GRAPHICAL ABSTRACT

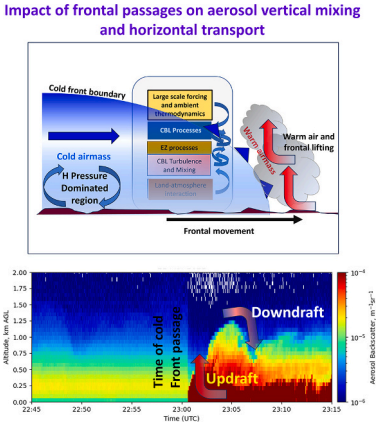

ARTICLE INFO

Editor: Pavlos Kassomenos

Keywords:
Aerosol transport
Atmospheric boundary layer
Cold fronts
Doppler lidar
Dryline
Semiarid region
Synoptic environments

ABSTRACT

Understanding the kinematics of aerosol horizontal transport and vertical mixing near the surface, within the atmospheric boundary layer (ABL), and in the overlying free troposphere (FT) is critical for various applications, including air quality and weather forecasting, aviation, road safety, and dispersion modeling. Empirical evidence of aerosol mixing processes within the ABL during synoptic-scale events over arid and semiarid regions (i.e., drylands) remains sparse. We explored how synoptic-scale weather systems impact aerosol mixing processes within the daytime ABL over a site located in a dryland. We used ground-based Doppler lidar measurements collected during three events: a cold-front passage, a fair-weather day, and a dryline passage over Lubbock, Texas. The measurements of backscatter and vertical velocity fields were obtained with temporal and vertical resolutions of 1 s and 60 m, respectively. Here, we documented observations of aerosol transport and mixing within the ABL and found that frontal passages are crucial for understanding ABL features and aerosol mixing processes. For example, our findings suggest that during a dryline passage yielding a water vapor mixing ratio drop of 10 g kg^{-1}, the boundary layer characteristics transition from being shallow and stratified throughout a

* Corresponding author at: Department of Geosciences, Atmospheric Science Division, Texas Tech University, Lubbock, TX 79409, USA.
E-mail addresses: Sandip.pal@ttu.edu (S. Pal), nec5299@psu.edu (N.E. Prince), michael.anand@noaa.gov (M. Anand), mhamel@ttu.edu (M. Hamel).

https://doi.org/10.1016/j.scitotenv.2024.178357
Received 12 October 2024; Received in revised form 17 December 2024; Accepted 30 December 2024
Available online 10 January 2025

stable, pre-dryline ABL aerosol regime (300 m deep) to a deep and well-mixed structure within the post-dryline ABL (2200 m deep) confirming a higher ABL depth growth rate (~300 mh^{-1}) than under quiescent conditions (~125 m h^{-1}). The results for the frontal case reported aerosol mixing via frontal lifting to an altitude of 1250 m from the ground due to strong updrafts (>7 m s^{-1}). Additionally, Doppler lidar measurements helped to characterize the aerosol mixing and transport processes in dry regions under different weather conditions which yielded close correspondence with the observed variability in near-surface particulate matter (i.e., $PM_{2.5}$) concentrations (e.g., increase in $PM_{2.5}$ from 9 μg m^{-3} to 27 μg m^{-3} due to a cold front passage). The aerosol transport, along with the derived properties of the mean up- and downdraft observations and variance-based (both vertical velocity and aerosol backscatter) turbulence profiling helped explain how frontal airmass exchanges impact aerosol loading near the surface. The results obtained emphasize the need to consider the impact of synoptic-scale events over drylands in both observational and atmospheric modeling studies.

1. Introduction

Aerosols play an essential role in several atmospheric and climate-relevant processes, including the radiation budget, cloud microphysics, convection initiation, cloud formation, and environmental pollution (Intergovernmental Panel on Climate Change, IPCC, Reinman, 2013). Additionally, the level of scientific understanding for both aerosol-radiation and aerosol-cloud interactions was reported to be either "low" or "very low" (i.e., Lynn and Peeva, 2021), and recent IPCC assessments documented that atmospheric aerosols are one of the most uncertain elements of the Earth's radiative budget (Forster et al., 2021).

The transport of diverse aerosols with different physicochemical properties can lead to health problems such as malignancy of lung epithelial cells (e.g., Yun et al., 2017). There is a strong need to address the concerns of human health resulting from poor air quality (AQ) under diverse weather conditions (e.g., Jhun et al., 2015). Consequently, resolving AQ issues for different atmospheric processes and relevant human health problems has been identified as a priority of the community and government. For instance, in the past two decades, the US AQ showed marked improvement; however, 40 % of the population still live in regions exceeding Environmental Protection Agency (EPA) standards (EPA, 2021). By improving our understanding of aerosol transport, resources can be developed and provided to at-risk populations impacted by potentially harmful aerosols. For these reasons, it remains essential to investigate aerosol transport processes across diverse synoptic and mesoscale meteorological conditions (e.g., Grini et al., 2005; Kassomenos et al., 1995; Vega et al., 2022).

The high spatial and temporal variability of atmospheric aerosol particles makes it challenging to obtain a comprehensive understanding of the vertical and horizontal transport of aerosols under different weather conditions in the lower part of the troposphere, in particular, within the atmospheric boundary layer (ABL, Pal and Lee, 2019a,b). The ABL is a critical interface trading mass, energy, and momentum between the surface and free troposphere (FT) via turbulence (Stull, 1988; Pal et al., 2013). Obtaining insights into aerosol transport in both vertical and horizontal directions within and above the ABL over arid and semiarid regions becomes even more challenging due to the aridity and abundance of dust (e.g., Achakulwisut et al., 2018).

While past studies noted deeper ABL depths in arid regions, they only accounted for the surface fluxes and entrainment processes, excluding the role of advection typically taking place during synoptic weather events. Only recently have researchers explored changes in ABL kinematics and thermodynamics due to different types of frontal environments (e.g., Pietersen et al., 2015; Clark et al., 2022; Anand and Pal, 2023; Walley et al., 2022). Moreover, during the passages of synoptic-scale weather systems (e.g., cold fronts, warm fronts, drylines, warm conveyor belts), complex aerosol mixing and transport regimes emerge yielding life-threatening incidents, such as hazardous driving conditions and poor visibility that led to vehicle pileups (e.g., Liu et al., 2021a, 2021b; Tong et al., 2023). In North America and many other parts of the world (e.g., subtropical southern Africa), drylines remain a critical airmass boundary for initiating convective processes (see, Scaff et al., 2021 for North America, and van Schalkwyk et al., 2022 for Africa). In general, drylines are airmass boundaries that separate flows of airmasses originating from very dry regions from humid and sub-humid regions generally characterized with much higher moisture content. In particular, in the Southern Great Plains of the US, drylines are formed frequently in spring and early summer months due to the merging of the westerly drier air from southwestern US and northern Mexico and moisture-rich southeasterly flow originated from the Gulf of Mexico (Hoch and Markowski, 2005). One should note that the drylines are closely associated with the presence of drylands (often called arid regions), being a major source of drier air due to low precipitation and low soil moisture content. According to Hulme (1996) and Huang et al. (2017a, 2017b), dryland areas mainly refer to the regions where the annual potential evapotranspiration (PET) remains much higher than the annual precipitation (P). An aridity index (i.e., P/PET ratio) <0.65 broadly defines drylands.

Aerosol transport associated with the changes in ABL dynamics during synoptic-scale events remains underexplored though critical for the rapidly warming climate of the 21st century (NASEM, 2018a, 2018b). Drylands are home to >3 billion people and cover roughly 41 % of the land mass on Earth (Safriel et al., 2005; Feng and Fu, 2013). In semiarid and arid regions, less soil moisture and sparse vegetation cover allow for stronger land-atmospheric coupling (Koster et al., 2004; Molod et al., 2019). As a result, there is less modulation of the ABL diurnal variability in semiarid regions compared to humid regions (Lee and Pal, 2017). Previous studies over semiarid and arid regions observed daytime ABL depths >4 km in northwest China (Zhang et al., 2005; Ma et al., 2011; Han et al., 2022) and up to 5.5 km in the Sahara Desert (Marsham et al., 2008).

Additionally, drylands are expanding due to climate change (Huang et al., 2016, 2017a, 2017b). This expansion yields concerns, especially from weather forecasting perspective. Since there is less process-based research work investigating ABL properties over drylands, numerical weather prediction (NWP) models do not perform as accurately as in other regions (Wehbe et al., 2019). For example, parameterization schemes struggle with the initialization of convection over semiarid regions (Couvreux et al., 2011; Wulfmeyer et al., 2018). Over drylands, across a range of land-cover types and meteorological conditions, the biosphere–atmosphere coupling is primarily linked to the energy partitioning (latent and sensible heat fluxes) and associated surface energy balance closure while soil moisture variability in these regions is extremely low pertaining to the low precipitation, high temperature, and strong windspeed favoring high evaporation rates. Consequently, land-atmosphere feedback processes become extremely complicated making parameterization of mean and turbulent structures of ABL thermodynamics challenging, which are decisive factors for convection initiation and cloud formation over land (e.g., Findell and Eltahir, 2003: Bhowmick and Parker, 2018; Lee et al., 2023). Previous work showed evidence that new observations help evaluate and develop model parameterizations and explore factors that govern the ABL thermodynamics on diverse temporal and spatial scales (Ma et al., 2011). Because a large portion of the Earth's population already lives in arid regions and the population growth of these regions is expected to increase due to dryland expansion, improving the parameterization schemes over arid

regions will benefit a significant number of the global population as well as a newer population base that may be at greater risk due to unforeseen changes in local climatology (i.e., humid to arid).

A detailed characterization of aerosol concentrations within the ABL on different timescales (e.g., diurnal, semi-diurnal, synoptic) remains highly uncertain (Pal and Haeffelin, 2015; Kokkalis, 2017; Hara et al., 2022). Complexities involved in the mixing and transport taking place in the ABL and their representation in numerical weather prediction models limit confidence in our understanding of the vertical and temporal variability of aerosol features during synoptically active and benign conditions (e.g., Zhang et al., 2009). We note that synoptically benign weather regimes mainly refer to the atmospheric conditions when they lack larger-scale kinematic forcing and any significant airmass exchanges; convective activity in this weakly sheared environment is mainly generated by local scale forcing (e.g., Bentley et al., 2010; Miller and Mote, 2018). On the contrary, synoptically active weather conditions refer to the environment where synoptic-scale processes dominate including the impact of frontal boundaries and associated rapid airmass exchanges with surface features including a synoptic-scale area of low pressure, among other factors (Hane et al., 2001; Burow and Ellis, 2021; Anand and Pal, 2023). Due to an increase in high-resolution observations using remote sensing instrumentations (e.g., lidar), observations of aerosol transport and ABL dynamics can be simultaneously retrieved during various weather conditions (e.g., Behrendt et al., 2005; Pal et al., 2008; Ma et al., 2020; Eck et al., 2020; Kokkalis et al., 2020).

The impact of frontal passages, including drylines, on trace gases, greenhouse gases, and aerosols has gained some consensus from the atmospheric science community, and an understanding of the processes and mechanisms has been recognized (e.g., Pal et al., 2020; Pal et al., 2021; Teixeira et al., 2021; Davis et al., 2021). But do the frontal passages have any significant impact on aerosol vertical and horizontal transport over arid regions where aerosol abundance is very high? How strong is the impact? What is the mechanism of influence during the airmass change that takes place during the passages of mid-latitude cyclones over land, in particular drylands?

We strive to answer the following key questions within this work: (1) How do the drylines impact aerosol mixing processes over an arid region site? (2) How do frontal passages and associated lifting impact aerosol temporal and vertical variability over a location? (3) Do the aerosol mixing processes differ between synoptically active and benign conditions? (4) What are the key advantages of using simultaneous measurements of aerosol features and ABL dynamics to obtain a broader understanding of aerosol vertical mixing and horizontal transport? To answer the above mentioned questions, a case study approach based on the simultaneous ground-based Doppler lidar measurements, near-surface meteorological observations, and nearby radiosonde launches over an arid region of West Texas in the US are utilized.

2. Experimental site, instruments, and datasets

2.1. Site: Reese Technology Center (RTC)

The experimental facility at the Reese Technology Center (henceforth referred to as RTC) in Lubbock encompasses a complex region at the interface of cold semiarid (BSk), hot semiarid (BSh), and humid subtropical (Cfa) climate zones (Beck et al., 2018), providing a unique opportunity to monitor meteorological conditions across distinct climate classifications. The land cover around the RTC site (Fig. 1a–b) is mainly characterized by shrub and scrub (e.g., grasslands and Herbaceous) while the soil type of the region is mainly dominated by Acuff loam (Soil Survey Staff, 2023). The region is characterized by frequently occurring passages of boundaries that distinguish maritime airmasses originating from the Gulf of Mexico from continental airmasses originating from northern Mexico. Moreover, due to low soil moisture, aridity, and sparse vegetation, the site is episodically impacted by the transport of dust from the west and southwest. The other key meteorological aspects that cumulatively define the weather features and climatological patterns of West Texas include frequent extreme temperatures (i.e., scorching summer and frigid winter), high variability in daily temperature range, frequent synoptic events, sustained high-wind regimes, low soil moisture caused by low annual precipitation (~500 mm), and severe weather systems associated with dryline passages (Kimmel et al., 2016).

2.2. Texas Tech Scanning Doppler Lidar (T^2-SDL)

The Texas Tech Scanning Doppler lidar (henceforth referred to as T^2-SDL, Fig. 1) was deployed at the RTC site in Lubbock in August 2021. The T^2-SDL typically operates in both vertically pointing and scanning modes and delivers three-dimensional wind and aerosol backscatter structures. The T^2-SDL, obtained from HALO Photonics, is a modular, autonomous, turn-key, pulsed Doppler lidar that makes remote sensing of motion and backscatter in the atmosphere (Vakkari et al., 2021). The lidar emits linearly polarized light through a transceiver aperture of 75 mm at a pulse rate of 10 kHz (resulting in 1 s resolution after a 10,000-pulse average during data acquisition) to observe targets that backscatter the transmitted pulses to the receiver. The receiver also can observe the Doppler shift brought about by the motion of the targets and, therefore, the radial component of their velocity. A large number of past studies reported the accuracy and reliability of HALO Photonics lidar system for diverse meteorological experiments (e.g., Hogan et al., 2009; Barlow et al., 2011; Huang et al., 2017a, 2017b). The T^2-SDL system allows radial velocity (and vertical velocity) measurement with an accuracy of -2.0 cm s^{-1} and velocity resolution reads 0.038 m s^{-1} with a velocity precision of <0.20 m s^{-1} for SNR > -17 dB. Also, while performing some tower-lidar intercomparison, we found mean wind speed difference (lidar-tower) in the ranges of 0.01–0.02 m s^{-1}. Regarding the aerosol backscatter signal intensity, since we used mainly variance profiles to estimate the ABL depth, the normalization in the variance signal provided us unique opportunity to explore the gradient from ABL to FT and we mainly focused on the relative changes in the backscatter coefficient while illustrating the impact of airmass exchanges on the aerosol field. Also, in the past, Tucker et al. (2009) and Pal et al. (2010, 2013) illustrated the accuracy of different techniques and reported that the vertical velocity variance and aerosol backscatter variance remains the most reliable technique to determine ABL depths with an accuracy of 50 m or less.

2.3. Other relevant meteorological datasets

We also used radiosonde measurements obtained from two sites: Amarillo, TX (35.23°N, 101.71°W, and 1094 m MSL), located in the middle of the Texas Panhandle and Midland, TX (31.94°N, 102.19°W, and 873 m MSL), located in the Permian Basin of the West Texas plains and approximately 387 km south of Amarillo, TX (Fig. 1a). The radiosonde profiles were obtained from the Integrated Global Radiosonde Archive (IGRA, Durre and Yin, 2008) for both sites. To characterize near-surface meteorological conditions, we used the measurements obtained at the West Texas Mesonet (WTM) site located within the domain. The WTM is an integrated atmospheric observation network of >155 stations, spanning a sizable portion of the arid-humid gradient of the West Texas region (105–99°W) and adequately covering the mesoscale boundaries (Schroeder et al. (2005). The WTM stations are equipped with aboveground standard meteorological sensors (pressure, temperature, wind, radiation, humidity) and belowground instruments for obtaining soil moisture and temperature at multiple depths. Table A1 in appendix provides some brief information on the accuracy and resolution of WTM sensors used in study.

Additionally, we also used the datasets for the daily air quality summary statistics reported by the US Environmental Protection Agency (EPA). Also, at a continuous ambient monitoring site (CAMS) maintained and operated by TCEQ (Texas Commission of Environmental Quality) in Lubbock (12th Street site, Site ID 4801028, 33.58°N and

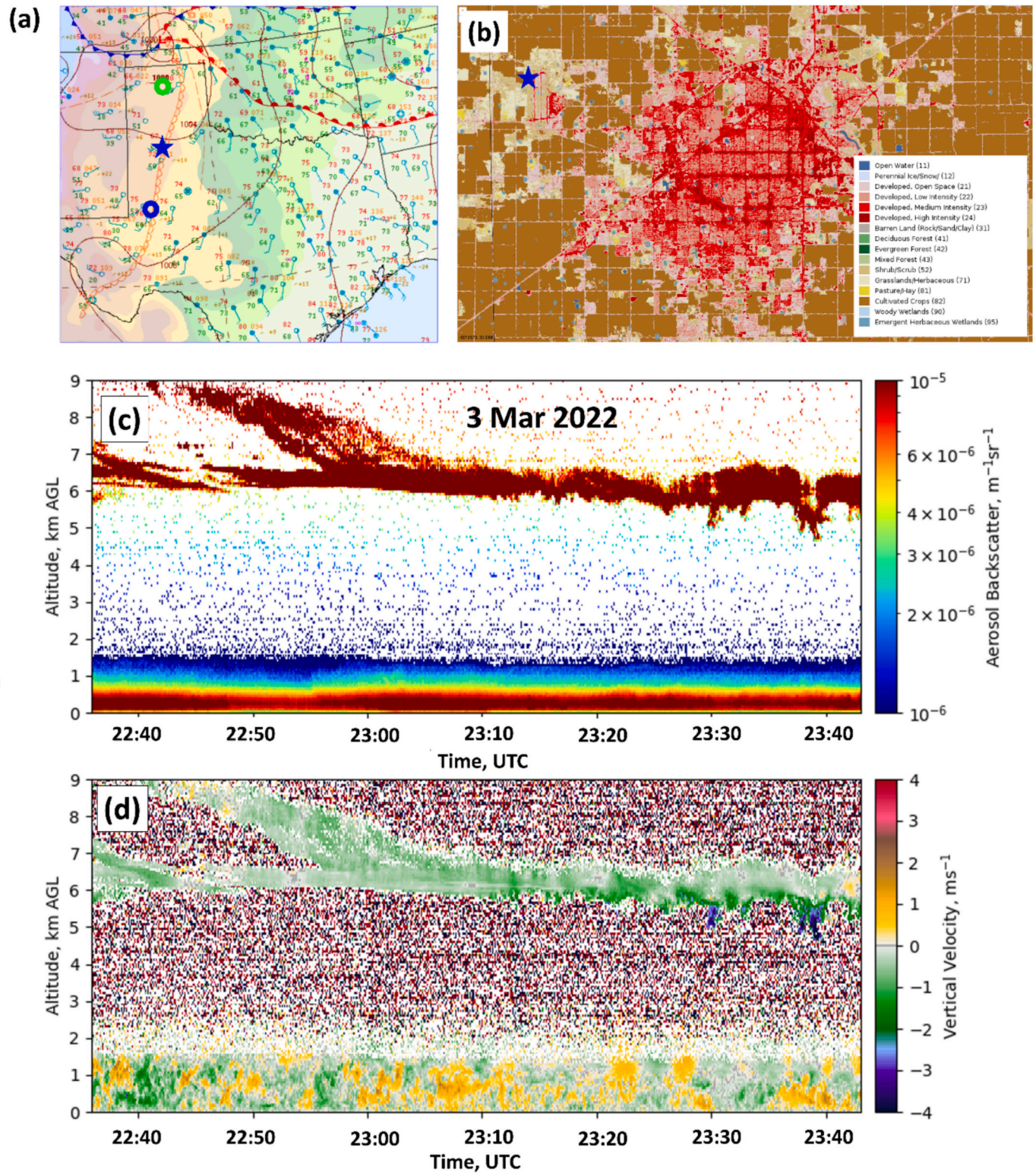

Fig. 1. Location of T^2-SDL measurement site at Reese Technology Center (RTC) near Lubbock (blue star) during the experiments and nearby upper air sounding sites (Blue circle: Midland; Green circle: Amarillo) overlaid on a surface chart analyses map (panel a). Land cover map surrounding RTC site (blue star) using annual NCLD (National Land Cover Database of U.S. Geological Survey) land cover data obtained MRLC (Multi-Resolution Land Characteristics Consortium) (b); city of Lubbock (red shaded pixels) is clearly visible. Time-height cross-sections of aerosol backscatter within ABL aerosol and cirrus structures (c) and associated vertical velocity field (d) at different heights (km AGL) obtained with temporal and range resolutions of 1 s and 60 m, respectively, over the measurement site on 3 March 2022.

101.78°W), routine aerosol measurements are performed using a Met One Instruments, Inc. BAM 1022 Real-Time Portable Beta Attenuation Mass Monitor which continuously measures the mass concentration of ambient particulate matter (here $PM_{2.5}$) collected onto glass filter tape with a time resolution of 1 min. This instrument (i.e., BAM 1022, https://metone.com) yields continuous (hourly) measurement of $PM_{2.5}$ with high accuracy, and minimal measurement artifacts and meets US-EPA Requirements for Class III $PM_{2.5}$ FEM (Federal Equivalent Methods for the US). The measurement range varies from 0 to 10,000 μg m^{-3} with measurement resolution of 1.0 μg m^{-3} while the lower detection limit is <4.8 μg m^{-3} (hourly, 2σ).

3. Prevailing meteorological conditions

We present selected measurements obtained from the T^2-SDL system deployed at RTC for three cases from late spring and early summertime: Case I- Cold-front passage during the late afternoon to early evening hours on 21 March 2022; Case II- Fair weather conditions on 28 April 2022; and Case III- Dryline passage during the late morning hours of 2 May 2022. For each case, we provided a brief overview of the synoptic setup based on both surface and upper air synoptic chart analyses and nearby radiosonde-based profiles of thermodynamic variables. We also analyzed the radiosonde profiles obtained over the two nearby upper-air sounding sites (i.e., Amarillo and Midland; see Appendix). For case I, radiosonde-derived profiles (Amarillo, Texas on 22 March 2022 00-UTC, i.e. 21 March 19:00 LT) of potential temperature and water vapor mixing ratio yielded ABL depth (z_i) of 0.5 km AGL most likely representing post-frontal boundary layer features (Anand and Pal, 2023). For case II, the radiosonde profiles from both Amarillo and Midland suggested the presence of a deep CBL with z_i of 4.0 km AGL which often occurs in the springtime over the experimental region. Midland sounding evinced relatively moist-ABL (ABL-mixing ratio of 6–7 g kg^{-1}) than over Amarillo (ABL-mixing ratio of 1.5–2.0 g kg^{-1}). Case III reported spatial variability in regional scale z_i as observed by the soundings over both Amarillo and Midland yielding z_i of 1.0 km and 2.3 km AGL, respectively.

3.1. Case I (21 March 2022)

In general, the synoptic conditions from 20 to 23 March 2022 surrounding the experimental region favored a significant amount of strong wind, periods of fire weather conditions, pockets of rain, and storms. In the low levels at 850 mb, backing southeast winds were observed in the region, allowing more moisture from the Gulf of Mexico to be advected into the region (Fig. A.5). Based on the meteorological measurements obtained at the Lubbock airport (KLBB, located on the northeast side of Lubbock), the dryline moved through the site around 16:00 UTC (11:00 LT) with a dewpoint change of 7.77 °C at 15:55 UTC to −1.11 °C at 17:15 UTC (Fig. A.6). However, we note that for the analyses presented in Section 4, we mainly used the collocated measurements obtained from the WTM site at RTC. During the afternoon hours of 21 March 2022, southwest winds were sustained at 9–11 m s^{-1}, gusting up to 18 m s^{-1}. The most intense storms formed along and ahead of a dryline over central and northern parts of Texas in the late afternoon and evening hours. The associated showers moved over the city of Lubbock, allowing stronger winds aloft to mix down to the surface and resulting in a wind gust of 22.8 m s^{-1} at 20:55 UTC. The entire experimental region was under the cooler post-frontal airmass by the next morning as the northerly flows established.

3.2. Case II (28 April 2022)

On the morning of 28 April (12:00 UTC), West Texas was located on the western edge of an upper-level ridge and under westerly-to-southwesterly flow ahead of an upper-level trough along the western Pacific coast (Fig. 2b). A dryline was backed into eastern New Mexico,

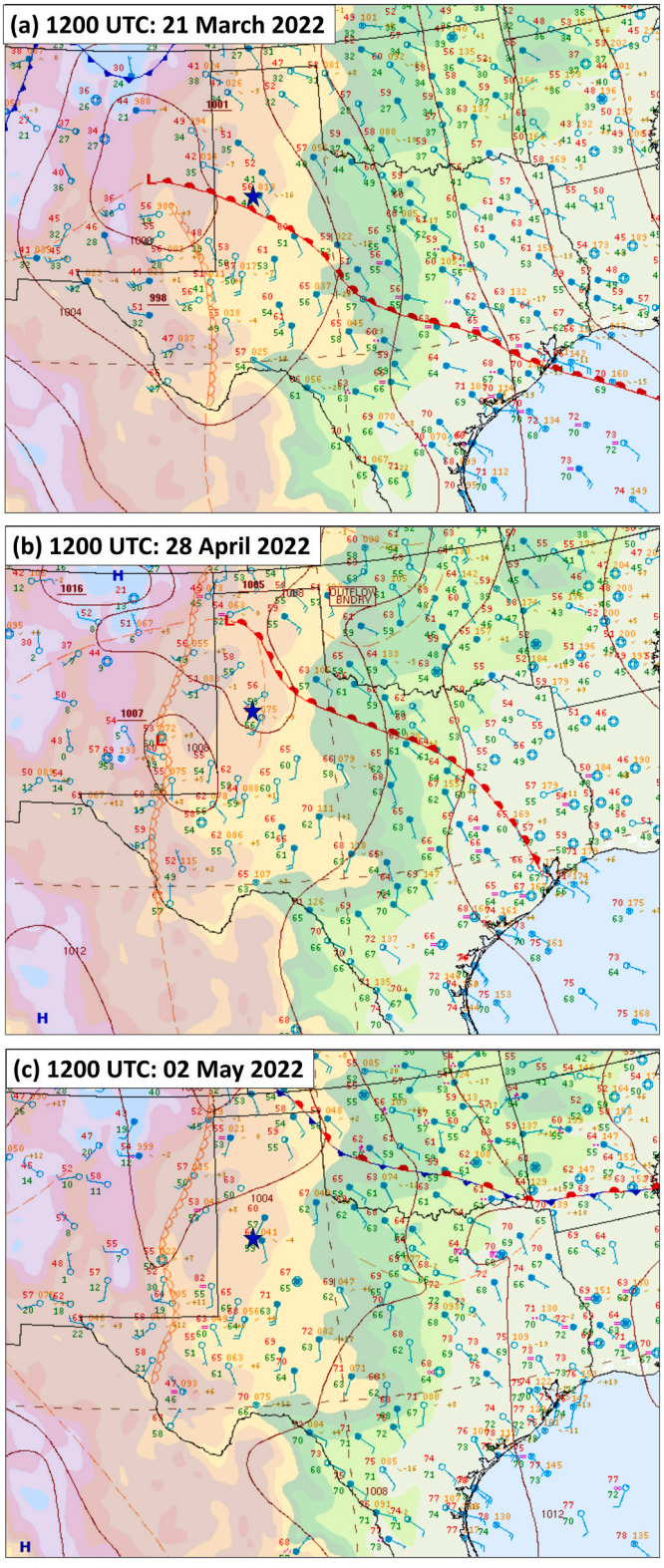

Fig. 2. Overall synoptic setup at 12 UTC on 21 March 2022 (a, case I), 28 April 2022 (b, case II), and 02 May 2022 (c, case III) using surface level analyses obtained from NOAA Weather Prediction Center (WPC). Blue star marks the location of RTC site near Lubbock, Texas. See Fig. A.7 in appendix for selected analyses of synoptic systems at 850 mb and 700 mb levels.

and a surface warm front was located across the Texas Panhandle, extending southeast into north and central Texas. High pressure centered in the southeastern US allowed southeast winds to advect low-level moisture into West Texas ahead of the dryline. The deep surface mixing behind the dryline allowed stronger winds aloft to mix down to the surface resulting in southwesterly winds at the surface. The RTC site and most of the Texas Panhandle were in the warm and dry sector west of the dryline by 00:00 UTC with moderate westerly winds aloft ahead of the upper-level trough axis in the Intermountain West.

3.3. Case III (2 May 2022)

On 2 May 2022, the experimental site was situated ahead of a dryline in the moist pre-frontal sector, with the dryline mixing east past the experimental site about 3 h into the measurement period. The experimental site was then under the post-dryline environment for the remainder of the measurement period. On the morning of 1 May 2022, the experimental region was located under an upper-level shortwave ridge in between a departing upper-level trough in the northern Mississippi River Valley and an incoming upper-level trough in the Pacific Northwest. By the morning of 2 May, the base of the upper-level trough was located in northeast New Mexico, progressing toward the east-to-northeast (Fig. 2). Surface winds began to veer to the southwest allowing the dryline to advance through eastern New Mexico into West Texas. Daytime heating and continuous southwest-to-west winds allowed the remaining low-level cloud cover to dissipate and the dryline to mix east past the experimental site in the late morning hours (Fig. 2c). The region was fully under warm, dry, southwesterly flow through the afternoon hours before a surface cold front moved south on the backside of the upper-level trough. This cold front moved through the northern and central Texas Panhandle during the late afternoon and early evening hours and through Lubbock and RTC shortly after sunset at 02:45 UTC on 3 May.

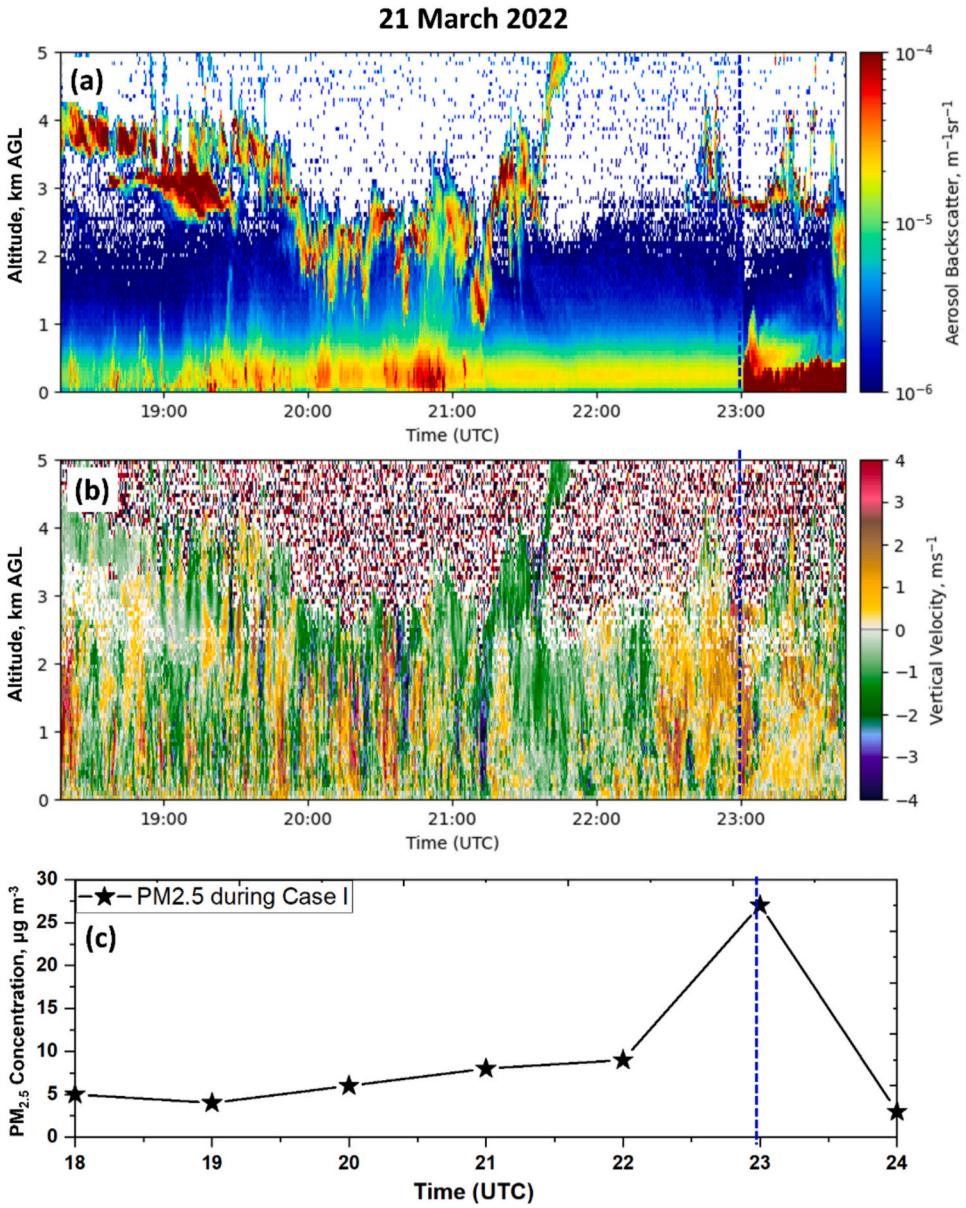

Fig. 3. Time-height cross-section of (a) aerosol backscatter (m^{-1} sr^{-1} × 10^{-6}); and (b) vertical velocity (m s^{-1}) obtained by T^2-SDL on 21 March 2022 for the entire measurement period from 18:38–23:45 UTC. (c) Temporal variability of $PM_{2.5}$ concentrations at the nearby TCEQ-CAMS site in Lubbock illustrating the impact of frontal passage on near-surface aerosol regime. The vertical dashed-blue line marks the time of cold-front passage over the site yielding a significant increase in dust concentrations over the entire experimental region of Lubbock.

4. Results and discussion

Based on the analyses of the EPA datasets, we found that all three cases were characterized by a low-to-moderate air quality index (AQI): 26, 51, and 52 during cases I, II, and III, respectively. Additionally, we found daily mean $PM_{2.5}$ (i.e., fine particles with diameters of 2.5 μm or less) concentrations of 8.47, 12.95, and 12.58 μg m^{-3} during cases I, II, and III, respectively. Fig. A.0 presents a brief overview of the $PM_{2.5}$

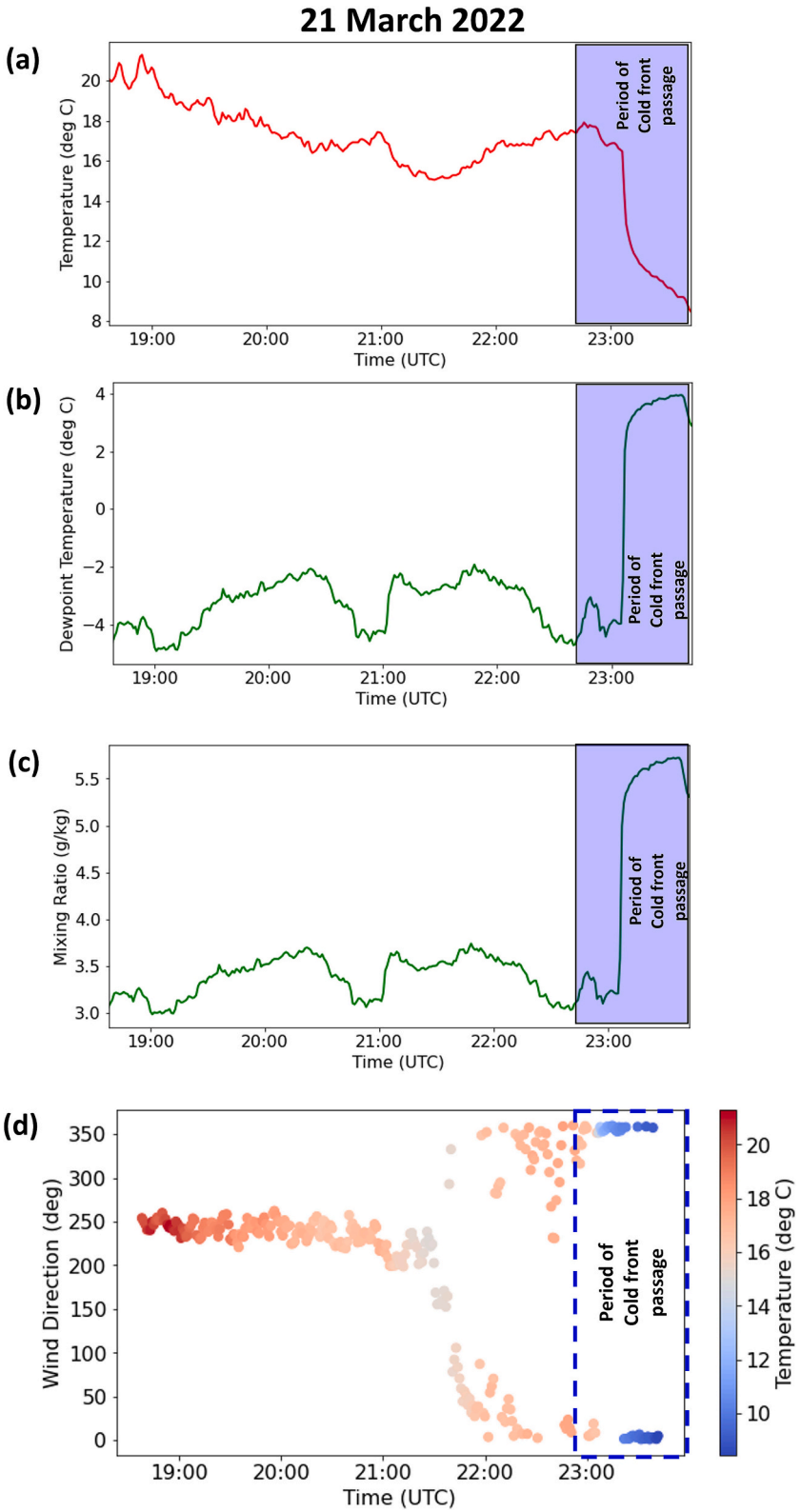

Fig. 4. Near-surface meteorological observations obtained from the WTM site at Reese Technology Center from 18:38–23:42 UTC on 21 March 2022 illustrating the changes in temperature (a), dewpoint (b), water vapor mixing ratio, (c) and wind direction colored with the observed temperature field (d, see color bar on the right) due to the cold-front passage over the site ~23:00 UTC as indicated by a shaded blue rectangle overlaid on each panel.

variability during the three cases.

While comparing the temporal variability in $PM_{2.5}$ before, during, and after each case, we found striking evidence that the passages of both cold front and dryline had a large impact on the $PM_{2.5}$ variability (see Fig. A.0 in appendix). For instance, on the day before the frontal passage of case I, measurements showed a large enhancement in the $PM_{2.5}$ concentrations (~55 μg m^{-3}) and remained high for >3 h while on the day of the frontal passage, we found another enhancement at the time of frontal passage at 23:00 UTC (18,00 CST) on 21 March 2022 (see panel (a) in Fig. A.0). During case II, $PM_{2.5}$ variability remained steady (daytime mean value of $PM_{2.5}$ of ~7–8 μg m^{-3}) and did not evince any enhancement which is a typical springtime value for the region.

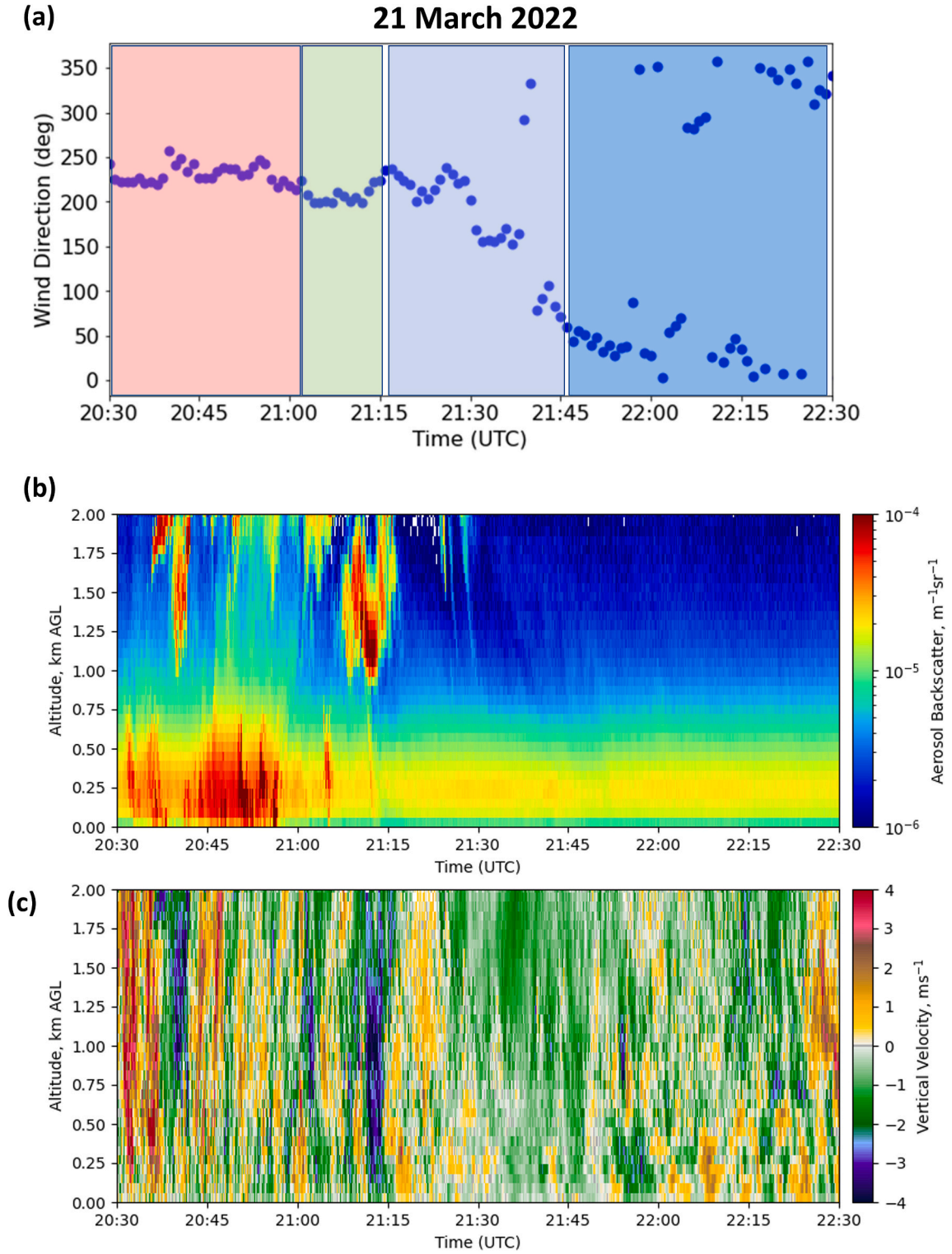

Fig. 5. Measurements of wind direction at 10 m using the observations obtained at the West Texas Mesonet site at Reese Technology Center (a) and a zoomed-in view of T^2-SDL measurements of vertical velocity (m s^{-1}) (b) and aerosol backscatter (m^{-1} sr^{-1} × 10^{-6}) from ground to an altitude of 1.2 km AGL from 21:00 UTC to 22:30 UTC on 21 March 2022 (c).

4.1. Case I: cold-front passage on 21 March 2022

4.1.1. Aerosol backscatter and vertical velocity fields

On 21 March 2022, the T^2-SDL measurements of aerosol backscatter and vertical velocity were acquired from 18:45–23:45 UTC (LT = UTC-5) at RTC (Fig. 3). Overall, the lidar measurements helped to obtain a visualization of the aerosol mixing during the course of the cold-front passage over the site yielding details on aerosol transport and stratification within the ABL before, during, and after the frontal passage. Instantaneous vertical profiles of aerosol backscatter and vertical velocity fields were obtained with a temporal resolution of 1 s and a vertical resolution of 60 m, as shown via the time-height cross-sections (Fig. 3). The time of the cold-front passage (23:00 UTC) is marked using a vertical dashed-blue line on each panel of Fig. 3. One should note that 23:00 UTC corresponds to 18:00 local time (i.e., LT = UTC-5) and typical sunset in March takes place around 20:00 LT; thus, the lidar measurements spanned during the daytime ABL regime. Fig. 3b also suggests the presence of a relatively strong updraft (vertical velocity ~2–3 m s^{-1} around 22:30 UTC (i.e., just before the cold front passage at 23:00 UTC) which could be attributed to an outflow boundary (i.e., mesoscale boundary separating thunderstorm-cooled air) as soon as the lift from the approaching system spread over from the west. One should also note that the most intense convective storms formed along and ahead of a dryline over parts of central and north Texas. Additional details on the impact of frontal passage on the aerosol environment and ABL kinematics are discussed in Section 4.1.3.

At the time measurements commenced, the site was behind the dryline but in the warm sector of the synoptic system with extensive cumulus cloud cover for most of the period due to the mid-level instability caused by the mid-level low in the Texas Panhandle (Fig. 2a). The near-surface meteorological conditions showed an air temperature of around 20 °C, mixing ratio of around 3.5 gkg^{-1}, and a dewpoint around −4 °C till 22:30 UTC (Fig. 4). The wind caused by the strong pressure gradient around a deepening low-pressure system resulted in a dust layer from the ground to an altitude of 700 m AGL, reducing visibility as illustrated in the time-height cross-section of aerosol backscatter fields (Fig. 3). Above the dust layer, a moderately strong aerosol field up to the lifting condensation level (LCL) at approximately 3 to 3.5 km was observed.

Higher aerosol concentration was consistently observed at the LCL throughout the period, indicating the presence of low-level cumulus cloud cover. The lidar measurements did not report any significant aerosol backscatter above those optically thick clouds. Additionally, the vertical velocity field suggested that the occurrence and fluctuations of cloud layers were highly associated with the presence of updrafts and downdrafts throughout the measurement period (Fig. 5). Additionally, lidar measurements also confirmed the presence of a large number of thermals and downdrafts and associated turbulent mixing of aerosols over the site. In particular, one downdraft that occurred just around 21:00 UTC (Fig. 5b–c) was most likely related to virga caused by the mid-level low and was associated with a slight decrease in temperature and an increase in dewpoint (Fig. 4b–c).

4.1.2. Changes in aerosol backscatter field via wind shift

During the measurement period of 20:30–22:30 UTC, the lidar measurements provided an opportunity to investigate the changes in ABL aerosol field due to backing (i.e., wind direction changing counterclockwise from south-southwesterly to north-northwesterly) as illustrated in Fig. 4d. For instance, from 20:30–21:00 UTC under south-southwesterly flows, we observed the presence of a deep aerosol layer with backscatter coefficients of $>5 \times 10^{-5}$ m^{-1} sr^{-1} at around 20:50 UTC (see Fig. 5b). Additionally, we also observed the presence of frequent and intense turbulent mixing of aerosols in the ABL around 20:30 UTC as updrafts (with w of >4 m s^{-1}, see Fig. 5c) were found to reach an altitude of 2 km AGL bringing the near-surface aerosol-laden airmass to the upper altitudes (Fig. 5b).

Between 21:00 and 21:15 UTC, the lidar site was still under the influence of south-southwesterly flows. However, a moderate decrease in aerosol backscatter coefficients (5×10^{-5} m^{-1} sr^{-1} to 2×10^{-5} m^{-1} sr^{-1}) was reported (see the green shaded region in Fig. 5a and reduced aerosol backscatter in Fig. 5b), presumably due to the presence of a strong downdraft around 21:12 UTC bringing cleaner aerosol-free air from the FT and presence of virga as mentioned before. Between 21:15 and 21:45 UTC, the lidar site experienced backing of the flows (i.e., SW-NE shift with wind direction changing from 220° to 30°, see the shaded light-blue region in Fig. 5a). This change in wind direction was associated with a strong downdraft in the vertical velocity profile (Fig. 5b). Consequently, lidar measurements also reported variable and moderately lower aerosol backscatter coefficients compared to the previous regime (i.e., between 20:30 and 21:15 UTC), in particular, from the ground to 0.5 km AGL.

Finally, the time-series plot of wind direction evinces that starting around 21:45 UTC, north-northeasterly wind prevailed over the site (see the shaded blue region in Fig. 5a). We note that shaded boxes in Fig. 5a were annotated based on the aerosol loading (qualitatively) so that shaded blue, light blue, green, and red represent very low, low, moderate, and very high aerosol loading, respectively, based on the findings reported in Fig. 5c. Additionally, during this phase, winds veered from northwesterly (at 21:40 UTC) to northeasterly (at 21:50 UTC), possibly due to the development of a surface low east of the region (Fig. 2c). Overall, the wind shift from south-southwest to northeast during the 1-hour period helped to advect relatively cleaner air from the east (i.e., the city of Lubbock) over the experimental site as seen by the lower backscatter values. Additionally, this resulted in a reduction in cloud cover after 21:50 UTC in the hour before the frontal passage, as seen by the aerosol backscatter profile (Fig. 5b).

Additionally, a schematic illustrating the impact of backing on the aerosol loading over the site is presented (via colored wind vectors) in Fig. 6b, where we used the identical color schemes as used in Fig. 5a. Overall, the analyses presented in Fig. 6 provide a composite view on the surface synoptic setup, changes in wind direction observed at different periods discussed in Fig. 5, and a satellite map qualitatively yielding the land-cover changes in a regional context. Previously, Pal et al. (2014) reported diurnal changes in aerosol concentrations in a valley site in central Virginia pertaining to the regular changes in up-valley versus down-valley flows and associated changes in wind directions under synoptically benign conditions. Also, recently, Takashima et al. (2019) and Pozo et al. (2019) investigated the impact of local front systems associated with typical sea-breeze and land-breeze regimes on stepwise changes in aerosol and trace gas distributions. However, to the best of the authors' knowledge, the example measurements presented here provide the first empirical evidence of the impact of the changes in synoptically induced flow patterns on the variability in ABL aerosol loading over an arid region.

4.1.3. Frontal lifting and ABL aerosol field

The interaction between the synoptic weather system and the ABL aerosol field remains another underexplored area in the field of aerosol research. In a number of past studies, surface network observations provided details on the nature of frontal passages and associated thermodynamic conditions and frontal lifting mechanisms (e.g., Taylor et al., 2005; Sinclair, 2013; Campbell et al., 2020). However, empirical evidence on the ABL aerosol mixing and transport due to frontal lifting remains sparse in the literature.

During Case I, the lidar observations provided some comprehensive details on the impact of frontal lifting on the ABL aerosol field, as illustrated via a zoom-in view of the time-height cross-sections (i.e., measurements covering the period of 22:45–23:15 UTC and altitudes ranging from 0.1 to 2.0 km AGL) of both aerosol backscatter and vertical velocity profiles (Fig. 7). The yellow-dashed line in both panels marks the time of frontal passage based on the findings of the temporal variability of near-surface thermodynamic variables at the site (Fig. 4)

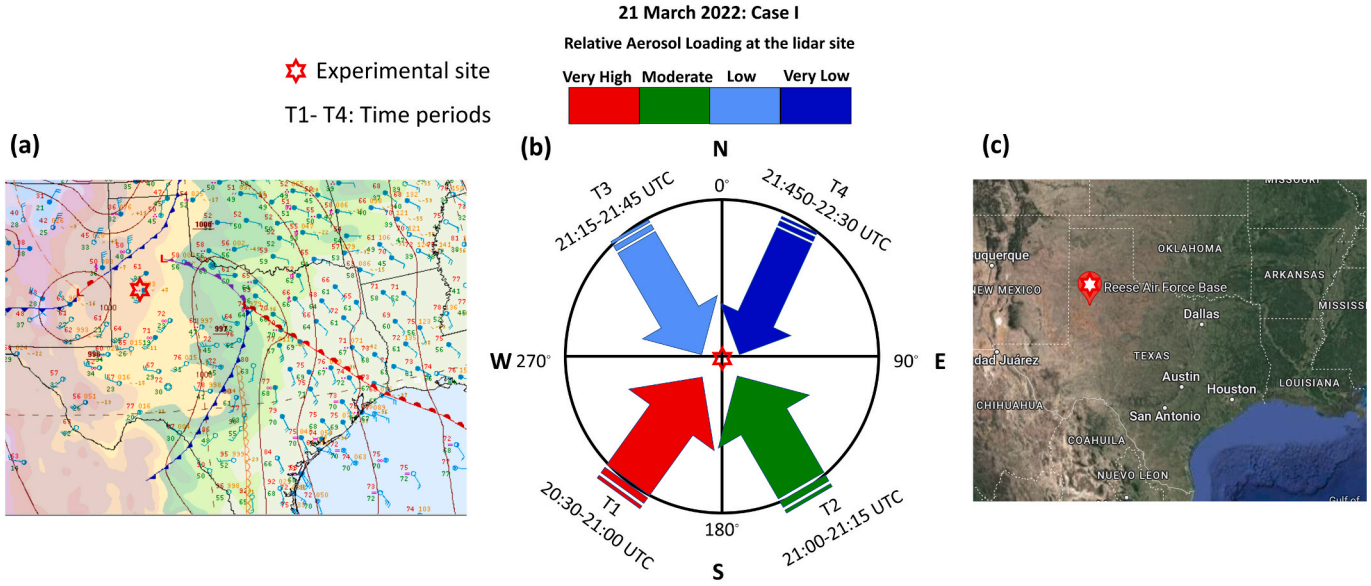

Fig. 6. Surface analysis at 21:00 UTC showing the development of lee low in central Texas (a). Red stars on all three panels indicate the location of the experimental site in Lubbock, Texas. A schematic depicting wind direction changes for four different periods and associated aerosol regimes (T1, T2, T3, and T4) caused by the development of the lee low (b). The red, green, light blue, and blue colors indicate the wind direction of SW, SE, NW, and NE, respectively, during the four periods, while the color bar matches the colors of the wind vectors illustrating four different aerosol loadings over the site obtained via lidar measurements (red: very high; green: moderate; light blue: low; and blue: very low on a relative scale). A satellite map depicting the overall terrain of the region with drier terrain to the west and greener terrain to the east of the experimental site (c, source of the image: Google Map).

yielding a sharp drop of 10 °C (from 18 to 8 °C) in temperature. Additionally, the measurements at TCEQ-CAMS site in Lubbock also reported a significant increase in $PM_{2.5}$ concentrations from 22:00 to 23:00 UTC time period (9 μg m^{-3} at 22:00 UTC to 27 μg m^{-3} at 23:00 UTC, Fig. 3c).

During the time of frontal passage over the site (~23:05 UTC), the lidar measurements reported the presence of strong updrafts (with *w* of 7 m s^{-1}) due to frontal lifting, while moderate downdrafts (with *w* of −2 m s^{-1}) were observed right afterward (23:08–23:15 UTC). These findings suggest that the vertical motion associated with the front was stronger in magnitude compared to the local thermals and downdrafts caused by surface heat fluxes and entrainment of FT air into the ABL. Additionally, lidar measurements provided strong evidence that cold fronts can impact ABL dynamics on a larger scale, confirming the frontal lifting of aerosols over the site. For instance, a strong dust plume was observed with aerosol backscatter coefficient values as high as 1×10^{-4} m^{-1} sr^{-1} during the passage of the cold front. This dust plume resulted in a depth as high as 1.25 km reducing visibility to less than a km (see the squares annotated on Fig. 7a and b for the aerosol structure and vertical velocity field, respectively).

The observed, dense aerosol plume was also associated with strong cold air advection and moisture advection. The WTM station at RTC observed a temperature drop from 16.55 to 9.85 °C between 23:05 to 23:28 UTC (Fig. 4a). During the same time, the dewpoint increased from −3.98 to 3.81 °C (Fig. 4b) with associated increase in water vapor mixing ratio (henceforth referred to as simply the mixing ratio) from 3.2 to 5.5 gkg^{-1}. At the Lubbock International Airport (KLBB, located ~45 km northeast of the lidar site), the temperature dropped from 17.78 to 10 °C and the dewpoint increased from −6.11 to 2.78 °C also during this time (not shown here). Wind speeds behind the front increased instantaneously due to an increase in surface pressure with sustained winds between 13 and 18 m s^{-1} and gusts of 26.38 m s^{-1} at 23:15 UTC.

Enhanced wind speeds caused widespread blowing dust and reduced visibility to 1 km near the end of the measurement period, yielding significant enhancement in the aerosol backscatter coefficients, in particular, from ground to 0.3 km AGL as reported by the lidar measurements (Fig. 7a). However, the temperature drop, and dewpoint increase due to the cold front were not associated with a wind shift to the north as northerly winds were already observed approximately 90 min before the frontal passage, as discussed before. This again could be due to the mid-level low in the Texas Panhandle causing surface cyclogenesis in central Texas.

The counterclockwise flow around the surface low resulted in northerly winds in the region before the cold-front passage. This is a common occurrence in the central US with pre-frontal wind shifts associated with lee troughing east of the Rocky Mountains, as was discussed previously by Schultz (2004), where they illustrated the mechanism for frontal passages with and without wind shifts.

Additionally, the vertical velocity became less strong (*w* decreasing from >4 m s^{-1} to 2 m s^{-1}) within the surface dust plume with stronger updrafts and downdrafts observed above the dust plume on the order of 2–3 m s^{-1} (Fig. 7b). This indicated that the cooler and more stable airmass advected over the site by the cold front resulted in less turbulent mixing and a more stable ABL profile due to elevated showers approaching the site. The lidar measurements were performed until 23:45 UTC as the showers generally washed out the aerosols present in the ABL, making it a challenge to determine aerosol backscatter using lidar measurements.

Overall, T^2-SDL observations during case I suggest that a cold front passage and associated changes in kinematics (e.g., presence of vigorous updrafts and downdrafts, strong windspeed) and thermodynamic conditions (e.g., large increase in moisture during the frontal passage with a sudden decrease in temperature) results in substantial changes in the overall ABL aerosol regime (e.g., a substantial increase in aerosol backscatter field, prevailing dust layer in the lower part of the ABL, lifting of the dust) over an arid region site in West Texas.

4.2. Case II: fair weather conditions on 28 April 2022

This case occurred during fair weather conditions on 28 April 2022 after a dryline passed over the Lubbock area around 18:00 UTC (Fig. 2b). There was no significant cloud cover throughout the measurement period on this day (19:30–00:32 UTC). Wind speeds measured at the Lubbock Automated Surface Observing Systems (ASOS) station at 18:00 UTC were light and variable. Measurements of dewpoint and mixing

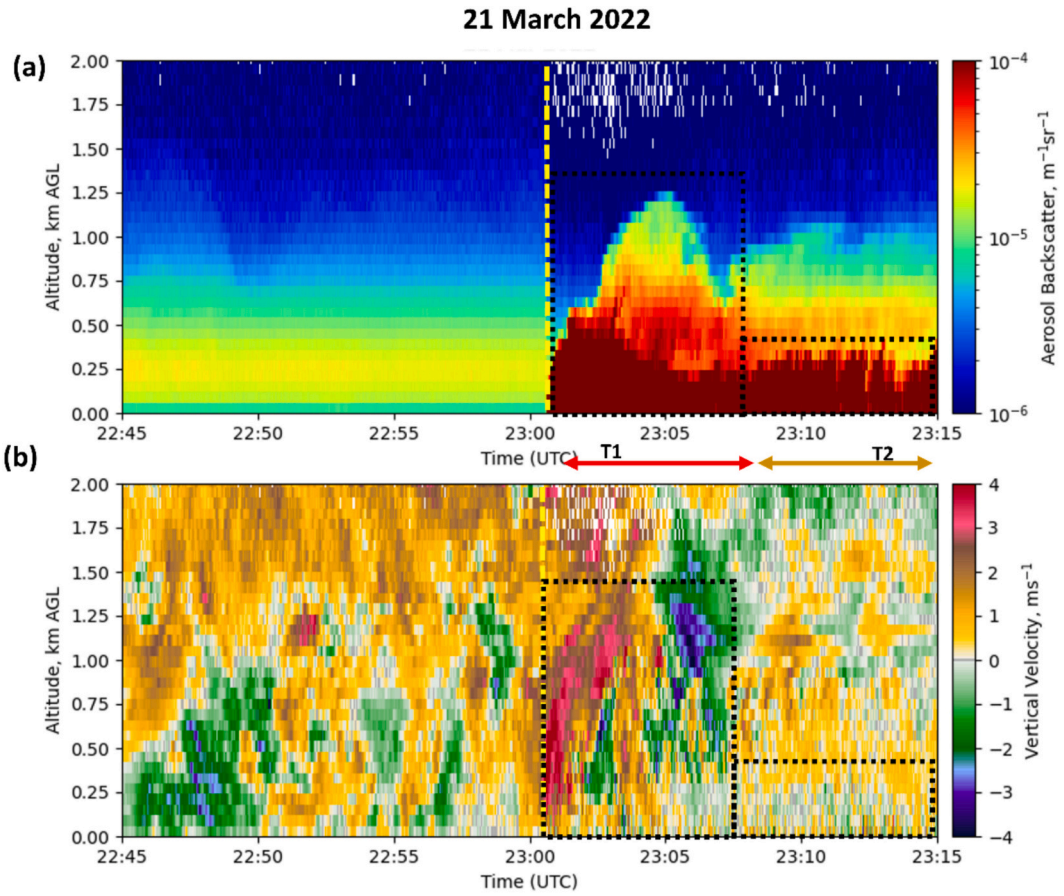

Fig. 7. A zoomed-in view of the time-height cross-sections of both aerosol backscatter (m^{-1} sr^{-1} × 10^{-6}) (a) and vertical velocity (m s^{-1}) (b) obtained via T^2-SDL measurements from 22:45 to 23:15 UTC centered around the time of the cold-front passage (23:00 UTC, marked by a vertical blue-dashed line) on 21 March 2022 illustrating an example of significant aerosol vertical mixing from ground to an altitude of 1.5 km AGL via the frontal lifting mechanism which was associated with a vertical velocity of up to 7 m s^{-1}. Note saturation of color bar beyond 4 m s^{-1} vertical velocity values. Two other rectangular boxes spanning the periods of T1 (23:00–23:08 UTC, marked by the red arrow) and T2 (23:08–23:15 UTC, brown arrow) indicate high and moderately deep aerosol loadings (panel a), respectively, and strong updraft and downdraft regimes, respectively (b).

ratio from the WTM site at RTC reveal the impact of the dryline passage on the near-surface thermodynamic conditions (Fig. A4 in supplementary materials). The results showed a steady decrease in dewpoint as the dryline passed over the site. The temporal evolution of the mixing ratio also depicted a similar downward trend.

Additionally, the lack of a sharp decrease in dewpoint and mixing ratio could be attributed to the fact that there was no significant convergence as southerly winds were observed on both sides of the boundary. Note that while the dryline passed before 18:00 UTC, there was little accumulated rainfall measured at RTC up until this time of the year, causing abnormally dry conditions and revealing why a sharp decrease in dewpoint and mixing ratio was not observed. The thermodynamic profiles obtained in the late afternoon (i.e., 00:00 UTC on 29 April 2022) from the nearby upper air sounding sites confirmed the presence of a deep ABL regime over the entire West Texas region yielding ABL depths of 3.9 and 4.2 km AGL over Amarillo and Midland, respectively (See Fig. A2 in supplementary materials). Similar deep ABL regimes over the region were reported in past studies (see McGrath-Spangler and Denning for global analyses, Lee and Pal (2017) for continental analyses, and Anand and Pal (2023) for regional-scale analyses of ABL depths). Additionally, lower, and less variable temporal variability in $PM_{2.5}$ concentrations throughout the measurement period could be mainly attributed to the ABL dilution in a deep ABL.

The T^2-SDL measurements of aerosol backscatter and vertical velocity showed occurrences of episodic, strong, and deep thermals reaching up to 4 km with *w* peaks of 6 m s^{-1} (Fig. 8b). These strong updrafts could be primarily attributed to the presence of high sensible heat flux at the site and the presence of the extremely dry and warm airmass originating from the southwest prevailing over the entire region; for instance, the daytime maximum temperature was recorded to be as high as 34 °C while the mixing ratio within the ABL (panel a Fig. A.2) and near the surface (panel b in Fig. A.4) was found to be 1.2 and 2.0 g kg^{-1}, respectively, confirming a dry and warm surface layer. Additionally, as the strong thermals lifted near-surface aerosols upward within the ABL, significant amounts of aerosol plumes with high aerosol backscatter coefficients (~5 × 10^{-5} m^{-1} sr^{-1}) were also reported by T^2-SDL measurements (Fig. 9). In contrast, cleaner FT air (aerosol backscatter coefficients of ~2 × 10^{-6} m^{-1} sr^{-1}) was entrained via broad downdrafts.

During 20:00–20:30 UTC period, there were intermittent intervals of upward and downward motion indicating the presence of strong thermals within the ABL. Another feature present throughout the analysis is the coupling of updrafts and downdrafts, which indicate the presence of horizontal convective rolls (HCR) (i.e., 22:00–23:30 UTC) over the region. Since these measurements were taken after a dryline passage, the presence of HCR is expected based on past findings (Peckham et al., 2004; Buban et al., 2012). The strongest HCR occurs just before 21:30 UTC, denoted by large values of upward motion followed by lesser values of downward motion. When this strong thermal occurs, there is also an increase in aerosol backscatter.

A zoomed-in view of this event is shown in Fig. 9, covering observations from 21:00–21:30 UTC. For instance, during the presence of

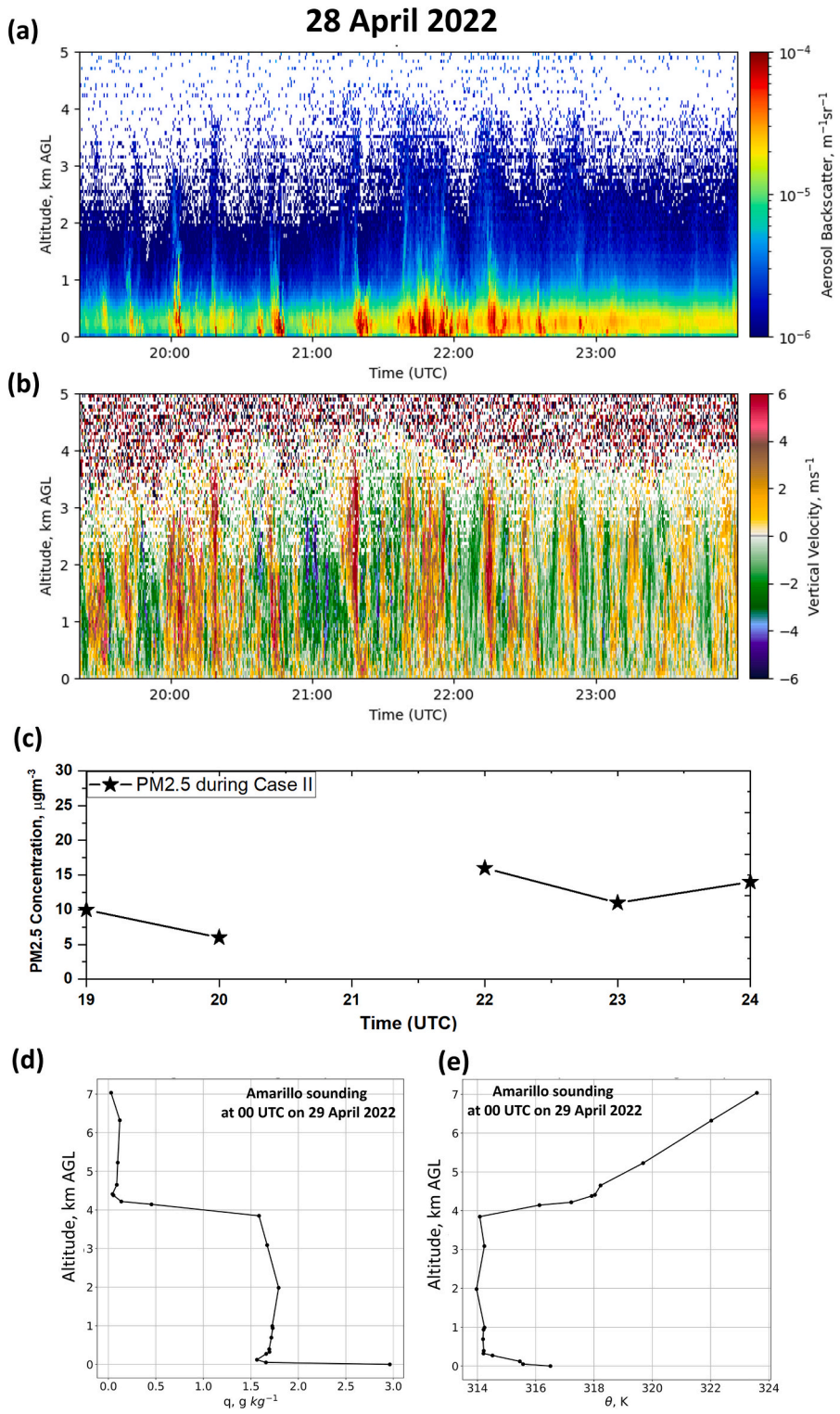

Fig. 8. Time-height cross-sections of aerosol backscatter (a) and vertical velocity (b) retrieved from lidar measurements on 28 April 2002. Temporal variability in hourly $PM_{2.5}$ concentrations observed at the nearby TCEQ-CAMS site in Lubbock (c). $PM_{2.5}$ measurements were missing around 21:00 UTC due to instrument malfunctioning yielding poor quality data which was screened during quality assurance and quality check processes. Vertical profiles of water vapor mixing ratio (d) and potential temperature (e) obtained from the 00:00 UTC sounding on 29 April launched from Amarillo, Texas, located 120 km north of the experimental site in Lubbock, illustrating a deep ABL scenario in the region with z_i of 3.9 km AGL; see supplementary document for details (Fig. A.2).

thermals around 21:18 UTC, a significant increase in aerosol backscatter within the lower 500 m of the ABL was observed. From 23:45 UTC until the end of the measurements, upward motions dominated the entire ABL regime. The thermals observed from the vertical velocity measurements on 28 April 2022 were strong and broad compared to the findings reported in previous literature (Lenschow and Stephens, 1980; Hogan et al., 2009), which could be a feature associated with an arid region site. Lastly, the strong thermals shown in Fig. 9 serve as an example of the vertical transport of aerosols from the surface into the ABL over an arid region site. Previously, while exploring spaceborne lidar

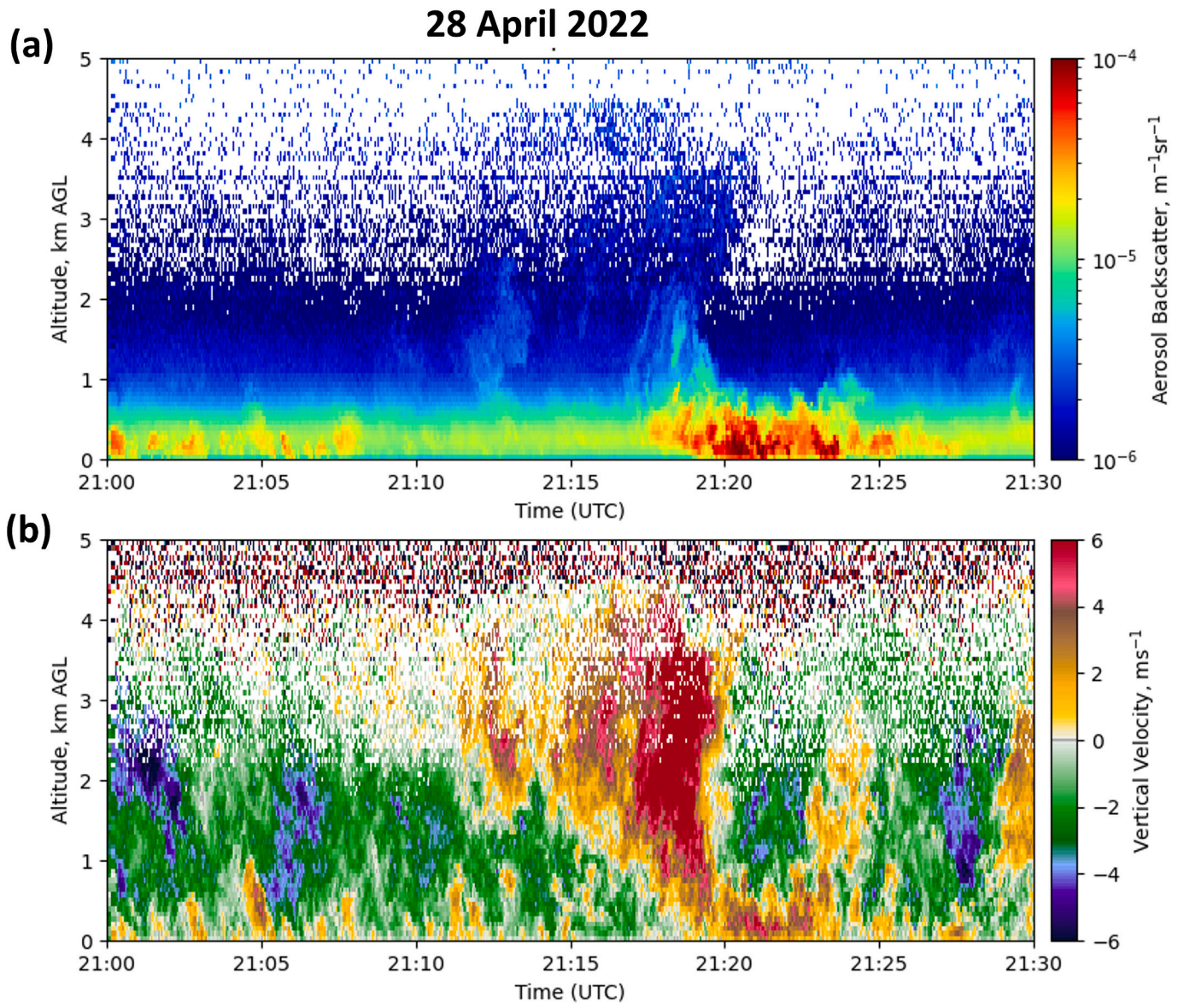

Fig. 9. A zoomed-in view of aerosol backscatter coefficient (a) and vertical velocity (b) during the presence of a deep, strong thermal that occurred just before 2130 UTC on 28 April 2022.

measurements over various parts of the globe, McGrath-Spangler and Denning (2013) found a deep ABL (>3000 m AGL) over the deserts in Africa, the Middle East, Asia, and Australia in summer. Additionally, using radiosonde-based analyses, Lee and Pal (2017) reported the presence of deeper ABL (>3500 m AGL) over the semiarid southwestern US throughout the year compared to the other climatic regions of the US. However, none of the past studies provided empirical evidence on the connection among ABL depth features, vertical transport of aerosols, and kinematics of thermals via vertical velocity field as reported here.

4.3. Case III: dryline passage on 2 May 2022

4.3.1. Aerosol backscatter and vertical velocity fields

The key aim for selecting case III (2 May 2022) was to investigate the impact of a dryline passage on the ABL aerosol mixing and transport. The T^2-SDL measurements acquired from 13:30–00:15 UTC (i.e., 08:30–19:15 LT) are shown in Fig. 10. During the first part of the lidar measurement period (i.e., from 13:30–15:00 UTC), the experimental site was ahead of the dryline with low-level moisture still present as indicated by the higher aerosol backscatter signal (Fig. 10a). The initial low-level cloud cover dissipated and moved east of the site just after 14:00 UTC due to the drier low-level southwesterly flow. This was indicated through the aerosol backscatter profiles, with lower values observed after 14:30 UTC. Temporal variability in aerosol measurements at the nearby TCEQ-CAMS site confirmed a steadily decreasing trend in $PM_{2.5}$ concentrations from 15 to 21 UTC (Fig. 10c) presumably due to (1) the wind shift from southwesterly to northwesterly bringing relatively cleaner air into the region; and (2) rapid growth of the ABL during post-dryline conditions allowing strong and rapid dilution and favoring ABL volume mixing (Stull, 1988; Pal et al., 2014).

Additionally, the thermodynamic profiles obtained in the morning (i.e., 12:00 UTC profiles of 2 May 2022, in Fig. 10d–e) and late afternoon (i.e., 00:00 UTC profile of 3 May 2022) over the nearby radiosonde site (Amarillo) showed a substantial decrease in the ABL mixing ratio (i.e., a decrease of about 5 g kg^{-1} (i.e., from 11 to 6 g kg^{-1}, Fig. 10d) due the passage of dryline over the entire region. The dryline passage occurred during 15:00–16:00 UTC on this day over the RTC site as marked by the brown shaded box overlaid on the time-height cross-sections of aerosol backscatter and vertical velocity in Fig. 10a and b, respectively.

In the beginning, the ABL over the site was relatively shallow (~600

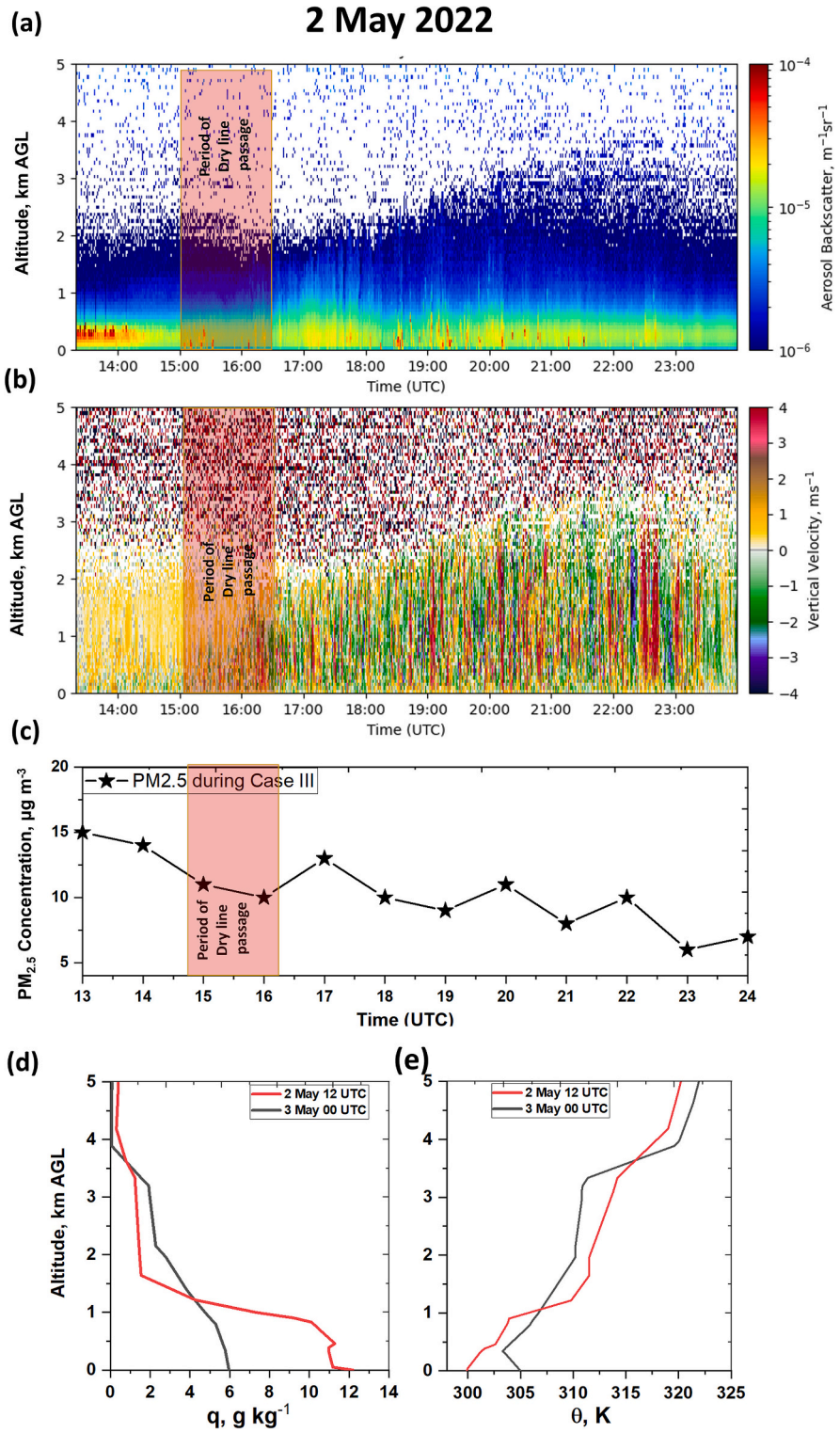

Fig. 10. Same as Fig. 3 but for aerosol backscatter (a) and vertical velocity (b) from 13:27 to 00:12 UTC during Case III (2 May 2022). Temporal variability in near-surface $PM_{2.5}$ concentrations at the nearest TCEQ-CAMS site in Lubbock. The shaded brown regions in all three panels mark the period of the dryline passage over the site. Vertical profiles of water vapor mixing ratio (q in g kg^{-1}, panel c) and potential temperature (θ in K, panel d) obtained via radiosonde launches at Amarillo (12:00 UTC on 2 May and 00:00 UTC on 3 May) illustrate the changes in q and θ in the ABL due the dryline passage in the region.

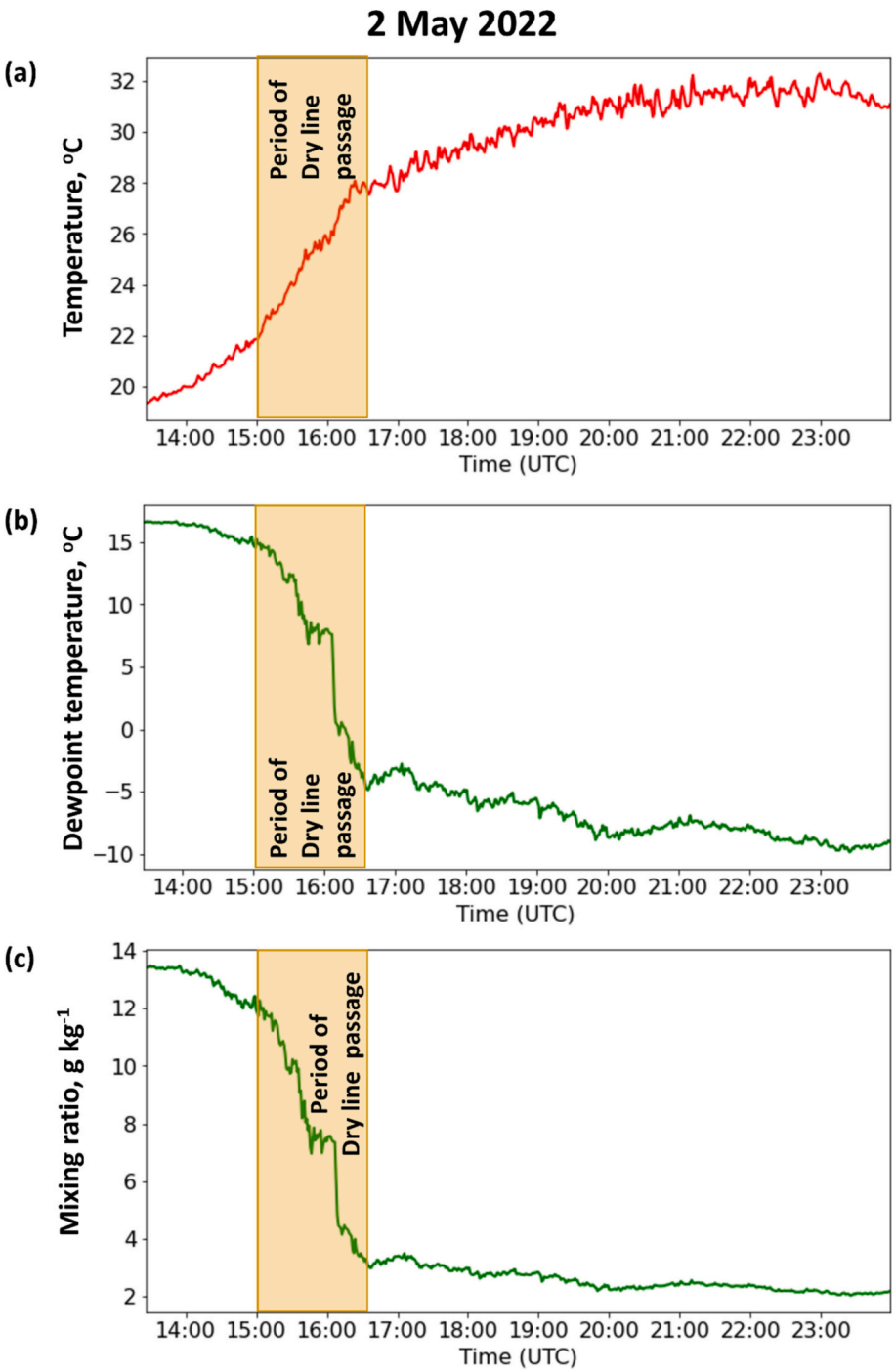

Fig. 11. WTM observation at RTC site from 13:30–23:30 UTC on 2 May 2022 illustrating the changes in temperature (a), dewpoint (b), and water vapor mixing ratio due to the passage of the dryline during the measurement period (15:00–16:30 UTC).

m AGL), with moderately high aerosol backscatter coefficients in the lower 500 m altitude (Fig. 10a) and without the presence of any significant updrafts until 15:30 UTC, indicating a more stable ABL during this time (Fig. 10b). It is possible that the low-level moisture ahead of the dryline resulted in reduced latent heat fluxes and thus limiting the growth of the ABL during this time. Before the dryline passage, there was a gradual growth in the ABL, with the ABL top heights approaching 1 km by 15:30 UTC, most likely due to surface heat fluxes increasing as indicated by rising surface temperatures (Fig. 11a). Thermals and downdrafts in the vertical velocity fields began to increase after 15:00 UTC possibly due to the beginning of drier air being advected over the site as the dryline approached from the west (Figs. 2c and 11).

4.3.2. Dryline passage

The dryline passage on this day was relatively gradual, as illustrated in Fig. 11. The brown shaded rectangular boxes overlaid on the time series of dewpoint (Fig. 11b) and mixing ratio (Fig. 11c) observations at the nearby WTM station indicated a dewpoint decrease from 14 °C at 15:00 UTC to −5.0 °C at 16:30 UTC) and a mixing ratio drop from 12 to 3 g kg^{-1} during the same time. These changes were also associated with a veering wind regime from the southwest in the pre-dryline sector to the west in the post-dryline sector (Fig. 12). It is worth noting that the frontal and dryline passages in the experimental region are typically shallow density currents and are heavily influenced by the complex terrain and nearby Rocky Mountains (e.g., Geerts et al., 2006; Bluestein,

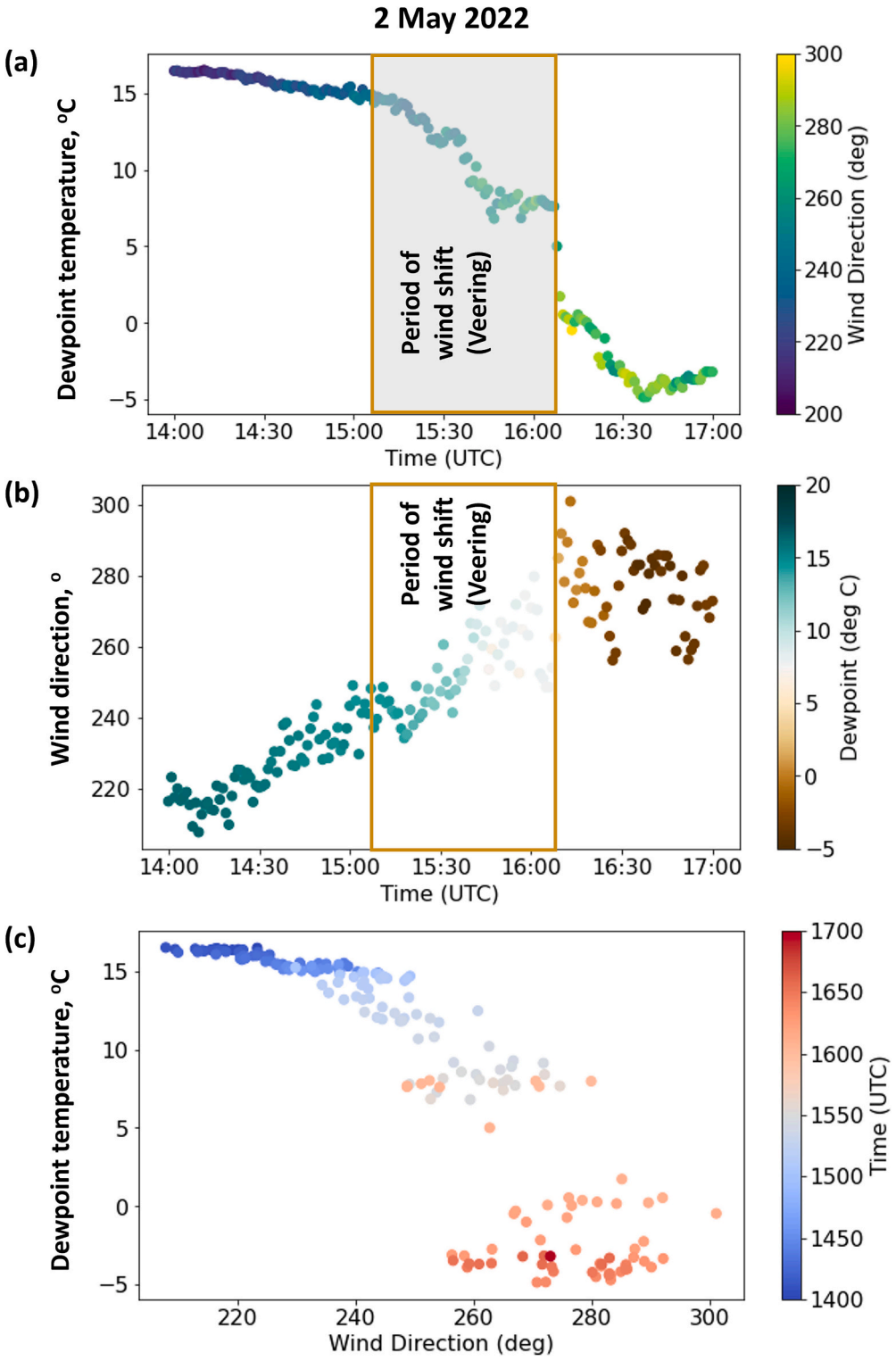

Fig. 12. The WTM observation at Reese Technology Center illustrating the changes in near-surface dewpoint (°C, panel a) and wind direction (b) from 14:00–17:00 UTC on 2 May 2022. The two brown rectangles mark the period of wind shift around the time of the dryline passage in the region. Dewpoint as a function of wind direction (in °) while colored symbols indicate time in UTC (panel c) indicating the simultaneous changes in dewpoint and wind direction at the site around 15:30 UTC.

2008) though this case indicated a gradual change in the near-surface thermodynamic features over a period of 1.5 h. Similar lidar studies could be conducted to investigate the impact of frontal passages on ABL aerosol fields over the eastern US or continental Europe since frontal passages in those regions behave more like synoptic-scale fronts, unlike the density currents over the southern Great Plains.

Another distinguishing feature is an increase in the magnitude of vertical velocity after the dryline passage at 16:00 UTC. Almost immediately after the dryline, there were more intense updrafts and downdrafts. Moreover, the thermals became deeper, reaching upwards of 1.5 km after 16:00 UTC, while in the pre-dryline sector, they were closer to 1.0 km in depth. The profiles of SNR (not shown) and aerosol backscatter coefficients (Fig. 10a) show higher aerosol loading within the first 500 m.

Both the fields of vertical velocity and aerosol backscatter coefficients during the passage of the dryline indicated the presence of stronger updrafts (w of 4–5 m s^{-1}), in particular, around 16:30 UTC (i.e., at the end of the dryline passage) as drier and warmer air established over the region. Isolating the effects of diurnal changes in heat fluxes and dryline passage on ABL aerosol mixing and associated dynamics would be an interesting future research topic. Nevertheless, based on past studies on dryline circulation, one would expect that the dryline helps promote the dry air aloft to mix down to the surface (Buban et al., 2007).

Additionally, large, and intense plumes of alternating updrafts and downdrafts every 5–7 min were observed in the post-dryline environment indicating the presence of horizontal convective rolls (HCRs), which have been noted in past observational studies (Peckham et al., 2004; Xue and Martin, 2006; Buban et al., 2012). The HCRs helped result in a more turbulent ABL mixing in the post-dryline environment (Fig. 10b). Near the end of the measurement period, there were instances of updraft regions reaching the top of the ABL. The updrafts and downdrafts within the ABL reduced in intensity at the end of the measurement period, indicating a reduction in surface heat fluxes as the sunset approached at 23:00 UTC.

Based on the overall observations from this day, it can be concluded that the dryline helped promote the transition from a stable stratified ABL in the pre-dryline airmass to a deep convective ABL in the post-dryline airmass. Another interesting observation from this case is that the ABL depth in the post-dryline airmass was shallower compared to the 21 March case. This might have occurred due to precipitation that fell across the region after an extended dry period. Even though the RTC did not receive any precipitation from convective activity on 1 May 2022, higher soil moisture in surrounding locations might have helped

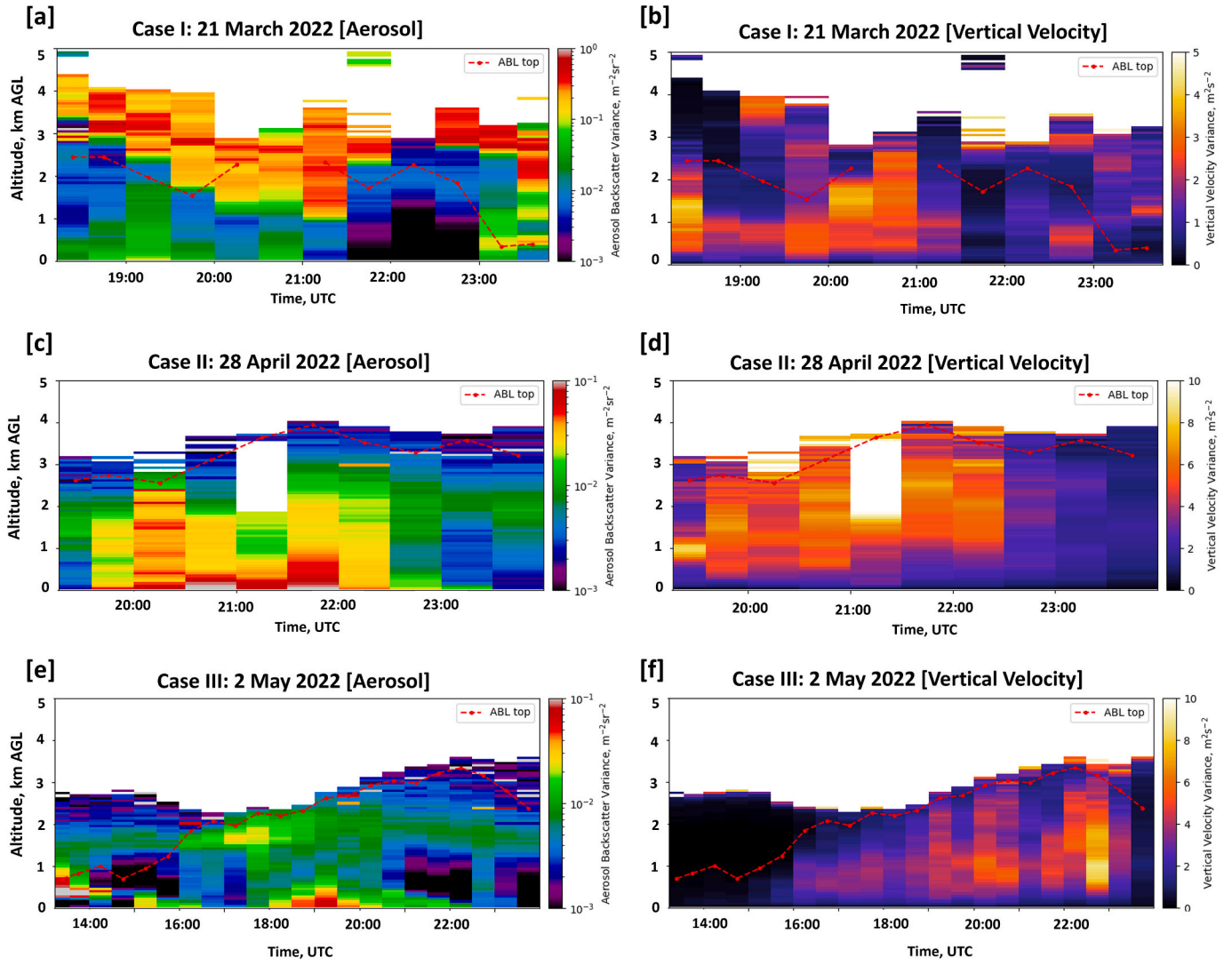

Fig. 13. Time-height cross-section of ABL-kinematics using both vertical velocity variance and aerosol backscatter variance estimated for every 30 min period for all three cases. Aerosol (vertical velocity) variance for cases I, II, and III are shown in panels a (b), c (d), and e (f), respectively. Variance-based ABL depths are overlaid (red dotted lines) on each panel illustrating remarkable variability among cases, and within each case pertaining to synoptic scale processes discussed in Section 4.4.

increase evaporation rates and introduce latent heat fluxes contributing to the shallower ABL depths. Additionally, the thermals observed on this day did not have as intense updrafts as seen on 28 April 2022, which is most likely due to rainfall on 1 May 2022 and a consequent increase in soil moisture and reduction in sensible heat fluxes.

4.4. ABL kinematics and aerosol turbulence mixing

The vertical velocity variance (σ_w^2) serves as an estimate of turbulent mixing within the boundary layer and is calculated using the vertical velocity measurements provided by the Doppler lidar. Numerous studies explored variance-based analyses (aerosols, water vapor, temperature) to determine mean ABL depths and illustrated turbulence features within the CBL (Tucker et al., 2009; Wulfmeyer et al., 2010; Pal et al., 2010, 2013; Behrendt et al., 2015). For each level, σ_w^2 was calculated across 30-min intervals. To provide a representative σ_w^2 within the CBL for each interval, σ_w^2 is averaged across $\frac{z_i}{2} \pm 100\,m$ (Clark et al., 2022; Clark, 2023). To identify the ABL top (i.e., z_i), a σ_w^2 threshold (0.1 $m^2\,s^{-2}$; Barlow et al., 2011) was used within a height range for each case. The minimum height for each case Is defined as follows: Case I: 250 m; Case II: 2250 m; Case III: 250 m. Note Case II's minimum height was increased because the σ_w^2 threshold was rarely met due to poor signal at the ABL top due to low aerosol content; hence, the minimum σ_w^2 above the approximate height of the maximum σ_w^2, in this case, 2250 m, was used instead. The maximum height for Case II was found to be 4000 m AGL, while the maximum height for Case I was 2500 m to avoid cloud interference in the retrieval. In case the 0.2 $m^2\,s^{-2}$ was not met, the minimum value in the profile, within the height range, was selected instead. The time-height cross-section of variance of vertical velocity and aerosol backscatter fields for all three cases (Fig. 13) yielded some distinct nature with respect to their turbulence processes while the z_i (overlaid on each panel) also showed significant variability among the cases. For instance, much deeper z_i was observed during case II and case III compared to case I as briefly discussed below.

Case I. The mean $\sigma_w^2(\frac{z_i}{2})$ leading up to the frontal passage on 3 Mar 2022 (18:00–23:00 UTC) was 1.97 m^2s^{-2} with an ABL top of 2070 ± 312 m, rounding to the nearest resolvable height. After the frontal passage (23:00 UTC), the variance dropped down to 0.505 m^2s^{-2}, and the ABL top decreased to 400 m. Notably, the σ_w^2 increased by about 0.986 m^2s^{-2} just before the frontal passage, after which σ_w^2 rapidly decreased by 1.17 m^2s^{-2} due to the increased stability behind the front.

Case II. The mean $\sigma_w^2(\frac{z_i}{2})$ on 28 Apr 2022 was 4.56 $m^2\,s^{-2}$ with an ABL top of 3210 ± 443 m, rounding to the nearest resolvable height. The maximum ABL top for this day was recorded at 3930 m at approximately 21:45 UTC, and the lowest was 2550 m at 20:15 UTC. The peak σ_w^2 was 6.26 $m^2\,s^{-2}$ at approximately 19:45 UTC.

Case III. The mean $\sigma_w^2(\frac{z_i}{2})$ before the dryline passage on 2 May 2022 (19:00–21:00 UTC) was 0.236 $m^2\,s^{-2}$ with an ABL top of 810 ± 123 m, rounding to the nearest resolvable height. During the dryline passage (15:00–17:00 UTC), the variance increased to 1.68 $m^2\,s^{-2}$, and the ABL top increased to 1530 m. Finally, after the dryline passage (17:00–19:00 UTC), σ_w^2 was 3.31 $m^2\,s^{-2}$, and the ABL top was 2190 m. For the remainder of the day (19:00–00:00 UTC), σ_w^2 was 4.04 $m^2\,s^{-2}$ with a peak at 22:45 CST of 7.21 $m^2\,s^{-2}$. The ABL for the remainder of the day was 2930 ± 282 m, with a maximum of 3330 m at 20:15 UTC. The temporal variability in vertical velocity variance around $z_i/2$ (i.e., $\sigma_w^2(\frac{z_i}{2})$) for all three cases (see Fig. A.7 in appendix) was also found to be very high while overall magnitude of $\sigma_w^2(\frac{z_i}{2})$ was found to be lower during case I compared to case II and case III. The high value of $\sigma_w^2(\frac{z_i}{2})$ during case III could be mainly attributed to the deep boundary layer and very high turbulence mixing within a dryline environment over arid region (Anand and Pal, 2023).

5. Overall discussion

The results presented in this work centrally focused on the exploration of the horizontal and vertical transport of aerosol within daytime ABL over a dryland ecosystem during three events under contrasting synoptic conditions (cold-front passage, fair weather, and dryline passage). Our findings suggested that frontal passages are crucial for understanding ABL features and aerosol mixing processes.

The first case (i.e., case I, 21 March 2022) helped to illustrate ABL aerosol transport and the evolution of ABL kinematics from the post-dryline, pre-frontal sector to the beginning of the post-frontal sector. All the findings for this case cumulatively suggest that cold front passage, associated meteorological conditions and front-relative kinematics (i.e., vigorous updrafts and downdrafts) had a significant impact on aerosol vertical and horizontal transport. For instance, the aerosol backscatter coefficients were found to be reduced by an order of magnitude (i.e., from 10^{-4} to 10^{-5} $m^{-1}\,sr^{-1}$) from ground to ~750 m AGL around 21:00 UTC due to the presence of virga. However, frontal lifting (strong updrafts, >4 m s^{-1}) yielded aerosol backscatter coefficients to once again increase by more than an order (0.6×10^{-6} to 5×10^{-4} $m^{-1}\,sr^{-1}$) and such aerosol loading sustained over the site for >30-min until the environmental conditions became hazardous and unhealthy due to strong gust and blowing dust. The elevated showers and virga resulted in strong downdrafts within the ABL and instances of shallower ABL depth of approximately 1 km, yielding a substantial increase in the aerosol backscatter coefficients in the ABL. Even though a substantial temperature drop, and moisture increase occurred due to the convergence, a wind shift occurred 90 min beforehand, potentially due to the development of a surface low east of the experimental site. Another observation to note is that the subsidence and advection of a shallow cold airmass behind the cold front did not impact the ABL aerosol field and kinematics until just before measurements were concluded.

The T^2-SDL measurements during case II (28 April 2022) provided details on the impact of surface forcing on ABL aerosol mixing processes during synoptically benign (quiescent weather conditions) regime when horizontal advection on ABL was negligible. For instance, results yielded frequent presence of deep and strong thermals up to an altitude of 4 km AGL over the site. These observational results suggest that over arid regions, deep thermals often reach the entrainment zone (here till 4 km AGL) during quasi-stationary ABL regime; finally, aerosol backscatter measurements also show evidence of thermals and aerosol-laden air reaching to the FT via strong updrafts (up to 6 m s^{-1}), thus, impacting the near-surface atmosphere.

Case III (2 May 2022) explored aerosol mixing and transport and associated ABL kinematics during a late morning dryline passage. During this part of the day, we found an increase in ABL depths and vigorous aerosol turbulent mixing due to the strengthening of updrafts and downdrafts as reported by the profiles of vertical velocity and aerosol backscatter variances. The dryline passage showed an increase in the ABL depth from 1 km AGL at 14:00 UTC to around 3 km at 17:00 UTC in a post-dryline environment, which was assisted by the presence of an elevated mixed layer from the adjacent plateau. Anand and Pal (2023) showed frequent presence of drylines and elevated mixed layer over the region during spring and early summer months. The observed increase in turbulent mixing allowed drier air from the FT to dilute the higher surface moisture near the surface and cause deep, strong thermals in the post-dryline environment. It is worth noting that this particular dryline passage was more gradual (i.e., a decrease in surface moisture occurring over a 60-to-90-minute period) than typical dryline passages in the region, which are more abrupt (Conder, 2005).

For brevity, we found it relevant here to discuss and answer the research questions posed in Section 1. Regarding the impact of drylines on aerosol mixing processes, our measurements showed that since the dryline passage took place during the diurnal heating period (16:00 UTC, i.e., 11:00 LT), the westerly drier air remained warmer than the

moist air in the east. For instance, WTM measurements showed the growth rate of near-surface temperature to be 6 °C h^{-1}. Additionally, 00-UTC soundings from the region confirmed a large dewpoint depression at 700 mb level (16 and 23 °C in Amarillo and Midland, respectively while further west in Albuquerque it was 26 °C) with low mixing ratio ranges of 1–2.8 g kg^{-1} above those sites. Under such dry, warm, and westerly and southwesterly flow regimes at both surface and upper air, a deep boundary layer had prevailed, which finally favored significant "volume mixing" of aerosols allowing strong entrainment of further drier and cleaner air from the FT above to the local ABL over the site. Finally, aerosol backscatter coefficients within the ABL were found to be (Fig. 10) lower compared to the other two cases (case I and case III). For case I, the results presented show the impact of frontal passages on ABL aerosol transport and mixing via strong westerly flow bringing aerosol-laden air at the lower level while frontal lifting facilitated making almost the entire ABL aerosol-rich. Also, the impact of pre-frontal wind shift on aerosol mixing was noted making the ABL cleaner due to the "fetch" effect transporting cleaner air from a region affected by recent precipitation.

We take this opportunity here to provide some additional insights on the applicability of the findings reported here to other arid or semi-arid regions. As recently reported by Dieudonné et al. (2024), more than a thousand Doppler lidars are operational around the world while $PM_{2.5}$ monitoring sites are also available in most of the sites or at location close to those sites; there exists huge potential for the application of the proposed framework to explore the impact of changing airmass boundaries over land on aerosol variability, in particular, over arid and semi-arid regions. For instance, Huang et al. (2014) provided some excellent reviews on the typical transport paths of aerosols over east Asian drylands; implications of airmass boundaries on those pathways could be explored for more insights into this topic. Sorooshian et al. (2011) demonstrated the potential of in-situ and columnar aerosol measurements to examine monthly trends in aerosol composition, aerosol optical depth (AOD), and aerosol size and characterized aerosol properties using meteorological measurements and back trajectory analyses in the southern Arizona region. However, airmass boundaries and associated kinematics were not explored in detail. We are convinced that airmass boundaries impact significantly the local ABL kinematics and thermodynamics which finally plays a vital role governing both local and regional scale aerosol variability. Thus, a huge opportunity exists when aerosol variability is explored using a lens of changing airmass boundaries over arid and semi-arid regions where dust remains abundant due to aridity, high wind, and extremely warm temperatures (e.g., Huang et al., 2017a, 2017b). In this context, we note that within NASA's AERONET efforts, we installed a Cimel Sun Photometer in June 2023 at RTC site for continuous daytime measurements of AODs and ongoing research suggests some important evidence on the impact of synoptic scale processes on AOD variability over the site (see Dhaliwal et al., 2023 for some preliminary results). In future, we will combine collocated measurements from Doppler lidar, Cimel and other in-situ sensors measuring $PM_{2.5}$ to explore additional details on the front-relative spatiotemporal variability in aerosol features.

We also note that while there exists a plethora of research work citing the implications of typical synoptic weather conditions on diverse meteorological phenomena including convection initiation, aerosol cloud microphysics, urban heat island, surface energy balance, carbon cycle, to name a few, their (i.e., synoptic-scale systems) impact on the variability in ABL aerosol field remained underexplored to a large extent over arid regions, mainly due to lack of routine robust measurements. Thus, it remained difficult to compare our findings with past work that are also based on Doppler lidar derived ABL kinematics and aerosol fields for exploring the impact of frontal systems including dryline passages on aerosol variability over dryland ecosystems. For instance, Takemi (1999) reported empirical findings while examining the impact of squall line on severe dust storm over an arid region in China. Their findings on the deep dry ABL in the pre-convective environment, frontal lifting, and horizontal transport of heavy dusts are similar (if not identical) in nature as the case I reported here. Also, Holben et al. (2018) using the Distributed Regional Aerosol Gridded Observation Networks (DRAGONs) provided some pathways to report the meso- and micro-scale aerosol features and processes across the world. Though synoptic scale processes were acknowledged, they did not discuss the critical role the airmass boundaries pose during the passages of mid-latitude cyclones on aerosol variability on diverse timescales. Also, Ledari et al. (2020) used satellite measurements and model simulations to document a frontal dust storm in west Asia and associated dry deposition; however, ABL aerosol processes were not discussed.

6. Summary, conclusions, and outlook

Within this work, we argue that frontal passages are often not explored yet crucial for understanding ABL features over arid regions, particularly changes in aerosol turbulent mixing and transport within the ABL. Using three case studies, we show evidence that the advection of ABL airmasses plays a critical role in aerosol transport and mixing over an arid region site in West Texas. Using Doppler lidar (i.e., T^2-SDL) observations of aerosol backscatter and vertical velocity fields as well as tower-based measurements of thermodynamics conditions and near-surface $PM_{2.5}$ concentrations, this work brings an important perspective to explore boundary layer aerosol mixing and transport in frontal environments. We provided observations demonstrating the capability of Doppler lidar measurements to characterize the process occurring to aerosol in dry regions under different weather conditions which yielded close correspondence with the variability of near-surface $PM_{2.5}$ concentrations. We explained how airmass exchange via advection is essential for a better understanding of aerosol vertical mixing and horizontal transport during both synoptically active weather conditions (e.g., across a cold front and dryline) and under a quasi-stationary ABL regime under fair weather conditions.

We conclude that the impact of cold front passages over drylands could pose health risks for humans and animals. Also, case I served as an example to comprehend the front-relevant impact and associated airmass change causing aerosol loading to change significantly within a short time (i.e., <5-minute time scale) over a dryland ecosystem. The observational findings reported here will help fill the gaps in our knowledge about aerosol transport processes and their roles in governing visibility in frontal environments which remained one of the most important factors causing poor environmental conditions, life-threatening incidents including road accidents, hazardous driving conditions, vehicle pileups, wind-blown dust, and dust storms, among others (e.g., Ashley et al., 2015). Additionally, the results could serve as a basis for examining dust emissions in arid regions (Klingmüller and Lelieveld, 2023).

Given the features of atmospheric aerosol mixing processes in active weather conditions over arid region is complex both due to the interplays of contrasting flows and the geographical characteristics, these results showed important features on the changes in aerosol regimes due to local boundary layer circulations impacted by the passage of synoptic scale weather systems. In particular, we introduced a novel conceptual framework for characterizing boundary layer aerosol mixing impacted by frontal environment over land. Additionally, this work shows some compelling evidence on how meteorological processes (e.g., dryline, frontal passage) and associate transport (e.g., airmass exchange via wind shift, enormous turbulent mixing via frontal lifting) impact changes in aerosol properties including aerosol concentrations and particle backscatter coefficient, and consequently visibility.

Finally, the findings reported will improve our understanding of the changes in aerosol regimes over arid regions of various parts of the world. Our work showed how to characterize aerosol transport before and after the dryline passages and how to determine, improve upon, and explain front-relative features in boundary layer aerosol mixing and transport processes toward building a comprehensive understanding of

the impact of advection on ABL aerosol regimes. Additionally, results illustrate that the T^2-SDL measurements have the capability of measuring time sequence profiles of vertical velocity and aerosol backscatter under both synoptically active and benign conditions and events and provide comprehensive details on the front-relative changes in aerosol mixing and transport in the ABL. We presented comprehensive discussion on the prevailing synoptic set up using surface chart analyses, collocated meteorological measurements from the West Texas Mesonet site, local weather station measurements from nearest airport and radiosonde launches from two nearby upper air sounding sites. However, application of reanalysis products (e.g., North American Regional Reanalysis, Mesinger et al., 2006) would be an important future asset to provide more details on the framework discussed and provide additional insights into the frontal passages in the region.

The measurement site is located in the downwind (under frequently observed westerly flows) of Mexican Plateau. Thus, the front-relative features in the ABL thermodynamics and associated changes in aerosol transport were also influenced by additional complex interactions under the presence of elevated mixed layer off the mountains and plateaus, which is also prevalent in the spring and summer months (Anand and Pal, 2022) but were not explored in this work. Additional measurements with west-to-east transact covering the entire West Texas domain with multiple lidars and $PM_{2.5}$ sensors would be beneficial in this regard. The framework used would need additional work before it is applied in mountainous regions to account for the impact of thermally induced flows (upslope, downslope, up-valley and down-valley) on aerosol variability (e.g., Pal et al., 2014). Additionally, the measurement site of $PM_{2.5}$ observations were located >8 km east of the lidar site, which remains another limitation of this work give spatiotemporal variability in aerosol particles, in particular, during synoptically active environment is generally very high as reported in some recent studies (e.g., Chen et al., 2023; Feng et al., 2023). Although the $PM_{2.5}$ measurements provided a general overview of the near-surface aerosol conditions, cautions need to be taken to directly relate these measurements to lidar measurements since measurement heights are different from each other: 1 m AGL for $PM_{2.5}$ and lidar measurement starts at ~90 m AGL. Another additional limitation was the poor temporal resolution of the $PM_{2.5}$ measurements presented here (i.e., hourly). We strongly believe that high-resolution measurements of PM_1, $PM_{2.5}$ and PM_{10} and particle size distribution of aerosols in this environment would be highly beneficial as reported in other studies (e.g., Sheih et al., 1983; Peter et al., 2010).

CRediT authorship contribution statement

Sandip Pal: Writing – review & editing, Writing – original draft, Visualization, Validation, Supervision, Software, Resources, Project administration, Methodology, Investigation, Funding acquisition, Formal analysis, Data curation, Conceptualization. **Nicholas E. Prince:** Writing – review & editing, Visualization, Validation, Software, Formal analysis, Data curation. **Michael Anand:** Writing – review & editing, Validation, Methodology, Formal analysis, Data curation. **Matthew Hamel:** Writing – review & editing, Validation, Methodology, Data curation.

Funding sources

This material is based upon work supported by the Observations Program within NOAA/OAR Weather Program Office under Award No. NA21OAR4590361. The co-author MH was supported by the Wind Science & Engineering (WiSE) fellowship while co-authors NEP, and MA were supported by the Graduate School at Texas Tech University. The lidar measurement facility T^2-SDL was developed using Texas Tech University's new faculty startup grant awarded to the lead author SP, while the work performed here was aimed to make the lidar system operational for field campaigns in 2022 and 2023 for the NOAA-funded project work.

Declaration of competing interest

The authors declare that they have no known competing financial interests or personal relationships that could have appeared to influence the work reported in this paper.

Acknowledgements

We highly appreciate the support of the researchers and staff members of the National Wind Institute, in particular, Dr. Brian Hirth and Dr. John Schroeder for providing the laboratory facility at the Reese Technology Center and West Texas Mesonet datasets, and Mr. Jeff Livingston for various supports during the experiments. Finally, we sincerely acknowledge the feedback and suggestions from the three anonymous reviewers which helped to improve both the technical and scientific contents of the manuscript.

Appendix A

The objective of this section is to provide additional information on the thermodynamic conditions in the experimental region during the three cases. We used nearby radiosonde profiles at different times (note UTC time) obtained from the two nearby National Weather Service Upper-Air Network sites, namely, Amarillo (35.23°N, 101.71°W, 1094 m MSL) and Midland (31.94° N, 102.19° W, 873 m MSL), located in the Permian Basin of the West Texas plains. These two sites in the Texas Panhandle region encounter extreme seasonal variability in temperature (seasonal temperature ranges of 28 °C and 27 °C for Amarillo and Midland, respectively). Midland is drier than Amarillo in terms of annual precipitation (NOAA/NWS, 2020; NOAA/NWS Midland/Odessa, TX, 2020).

Both Amarillo and Midland are located on flat terrain. Amarillo is located in the grasslands of Northern Texas and is surrounded by dense prairies. Midland is located in a large sedimentary basin, commonly referred to as the Permian Basin, encompassing western Texas and southeastern New Mexico. The radiosonde measurements and surface observations from the launch site are then compiled into a sounding profile and then distributed to local, regional, and national forecasting offices and agencies across the globe (Durre et al., 2006). One of these agencies, the National Climatic Data Center (NCDC), compiled quality-controlled radiosonde observations into a user-friendly, readily accessible dataset referred to as the Integrated Global Radiosonde Archive (IGRA, Durre and Yin, 2008). Using the radiosonde measurements, we showed the thermodynamics profiles obtained for case I (21 March 2022, Fig. A.1), case II (28 April 2022, Fig. A.2), and case III (2 May 2022, Fig. A.3). One should note that we used 00-UTC launches for the next calendar day (e.g., 00 UTC on 22 March 2022) as it corresponds to the daytime lidar measurements of 21 March 2022 (i.e., LST = UTC - 6 h). Additionally, Fig. A.4 shows the temporal evolution of near-surface thermodynamic conditions including temperature, dewpoint temperature, and mixing ratio from 1600 to 2248 UTC on 28 April 2022.

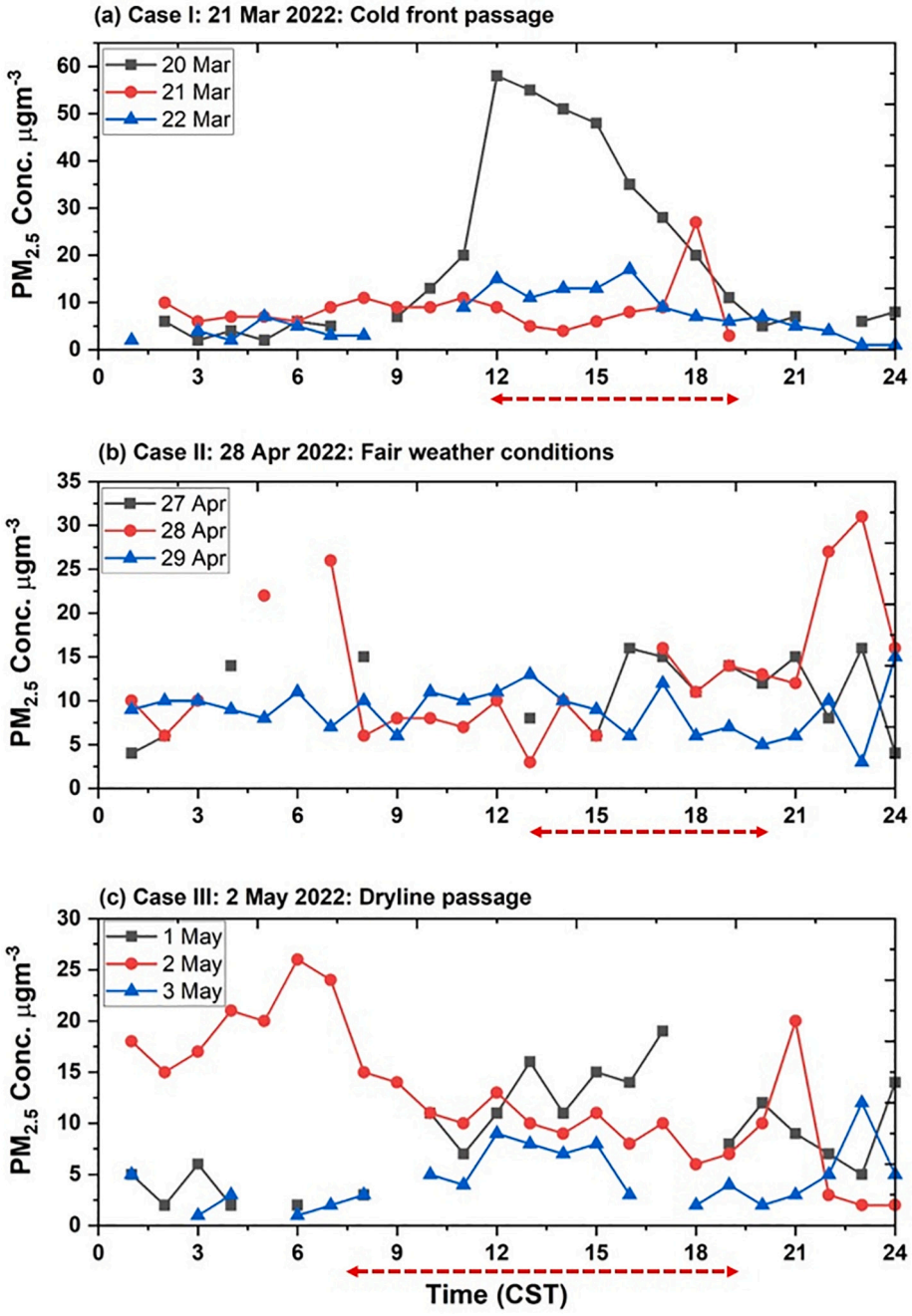

Fig. A.0. Temporal variability in $PM_{2.5}$ concentrations measured at the TCEQ-CAMS site in Lubbock during a three-day sequence centered around the day of case I (a), case II (b), and case III (c). Line and symbols in black, red, and blue mark the measurements on the day before, on the day, and after one day of the case study, respectively. The horizontally aligned red-dashed line along the x-axis on each panel marks the period of lidar measurements during the three cases.

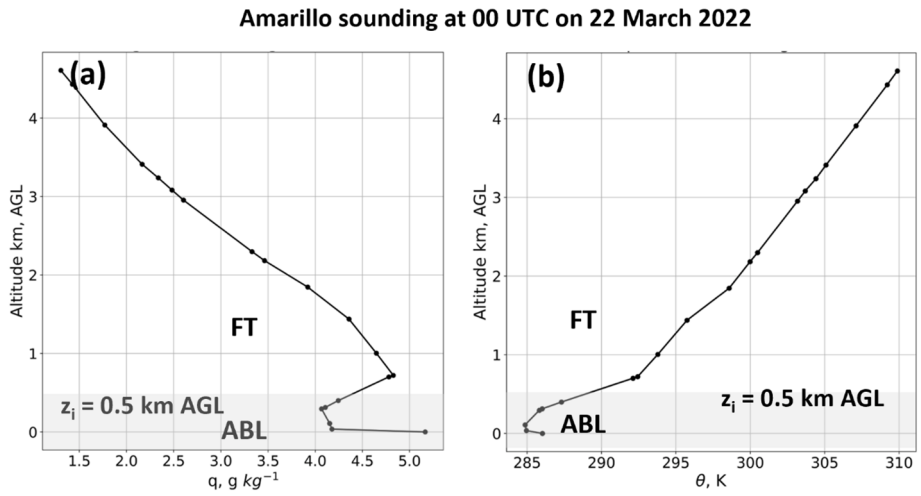

Fig. A.1. Overall thermodynamic condition using the radiosonde-derived profiles of water vapor mixing ratio (a) and potential temperature (b) obtained on 22 March 2022 over Amarillo. Panels c and d are same as panels a, and b, respectively but over Midland. z_i marked on each panel separates the ABL (shaded region) and overlying FT.

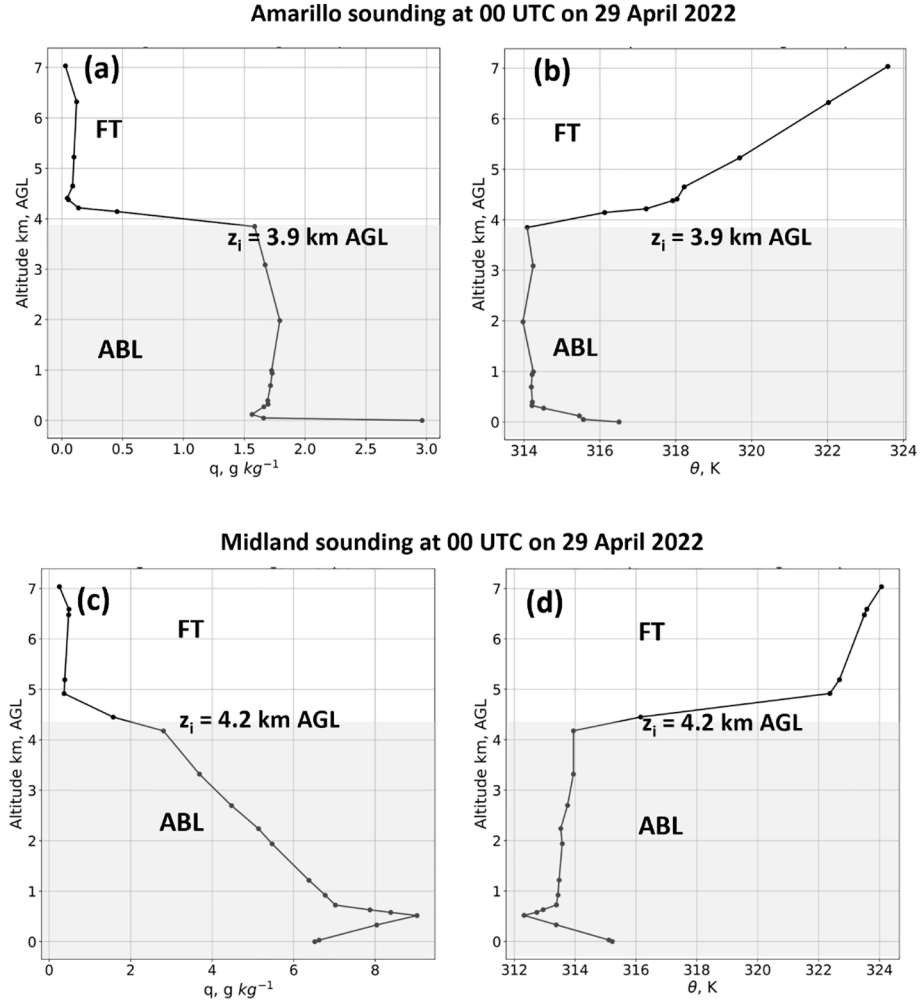

Fig. A.2. Same as Fig. A.1 but for 29 April 2022. Panels c and d are same as panels a, and b, respectively but over Midland. z_i marked on each panel separates the ABL (shaded region) and overlying FT.

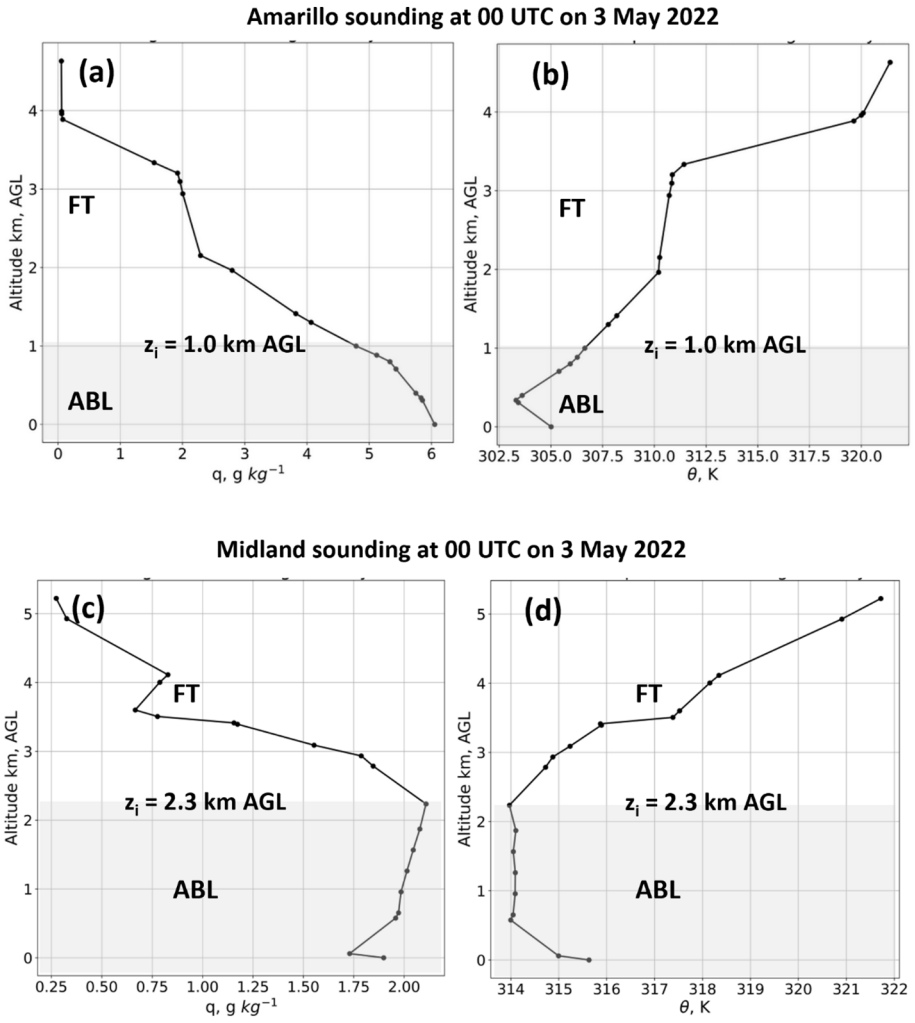

Fig. A.3. Same as Fig. A.1 but for 3 May 2022.

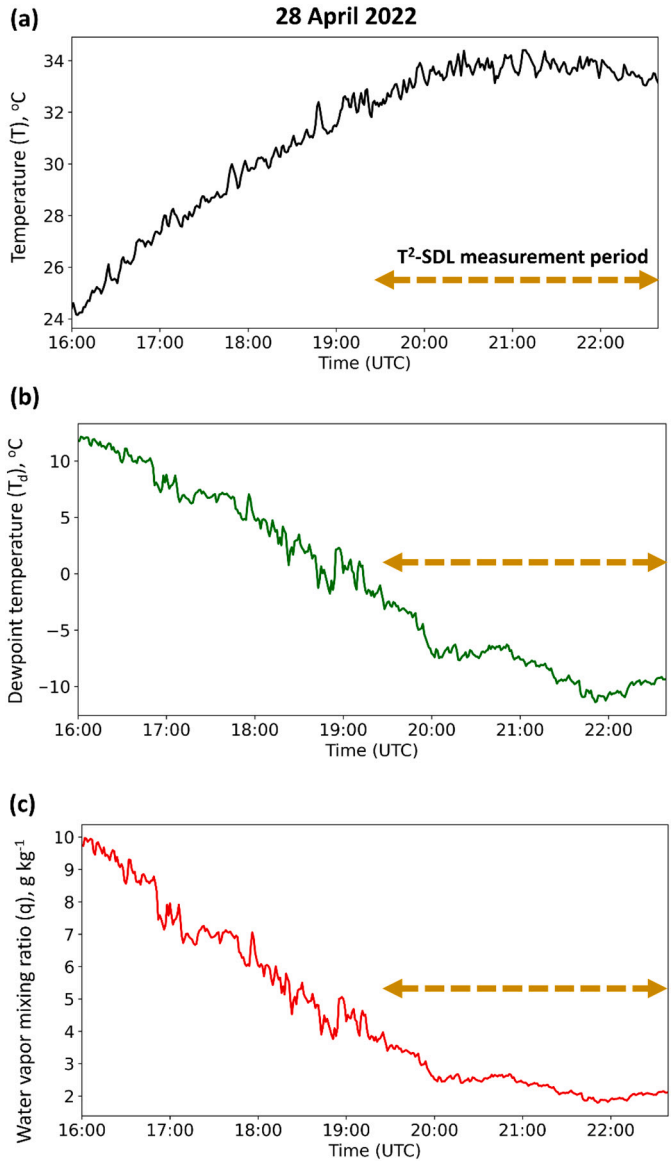

Fig. A.4. Temporal evolution of temperature (a), dewpoint temperature (b) and mixing ratio (c) from 1600 to 2248 UTC on 28 April 2022 using the observations obtained at the West Texas Mesonet (WTM) site at RTC. Dashed brown arrows mark the period when T^2-SDL measurements of aerosol backscatter and vertical velocity field were made in a post-dryline fair weather environment.

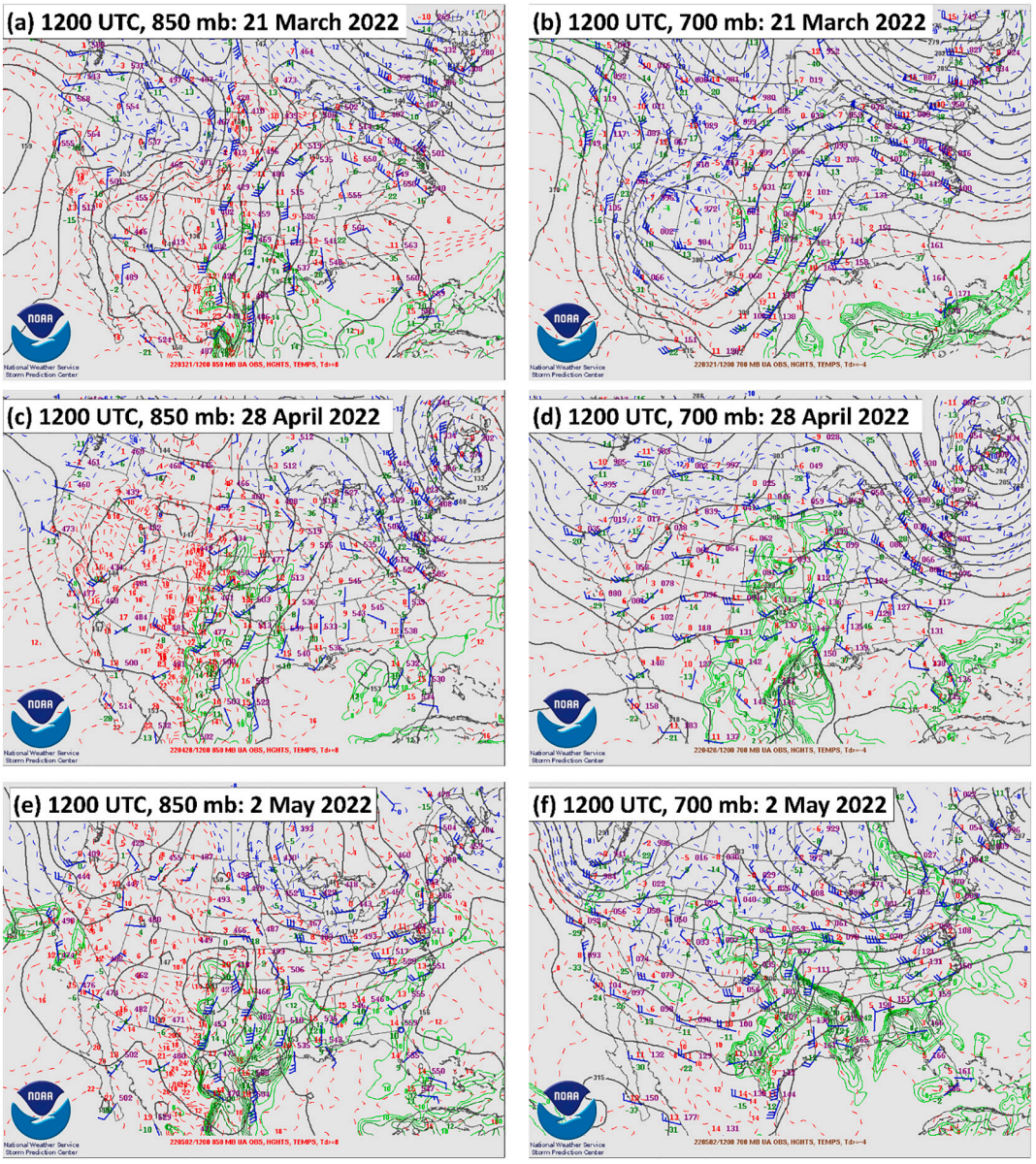

Fig. A.5. Synoptic set up at both 850 and 700 mb levels across the US for the three cases (a and b for case I, c and d for case II, and e). Source: Storm Prediction Center. https://www.spc.noaa.gov/obswx/maps/.

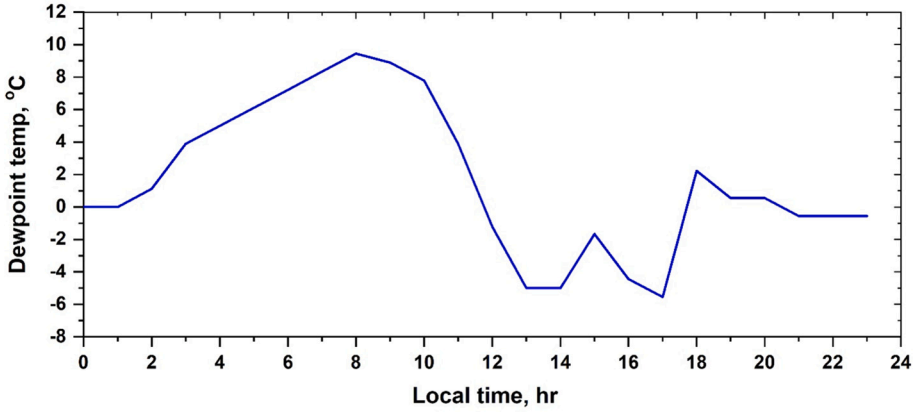

Fig. A.6. Temporal evolution of dewpoint temperature (°C) measured at Lubbock International Airport ASOS site illustrating the dryline passage between 11 and 12 LT on 21 Mar 2022.

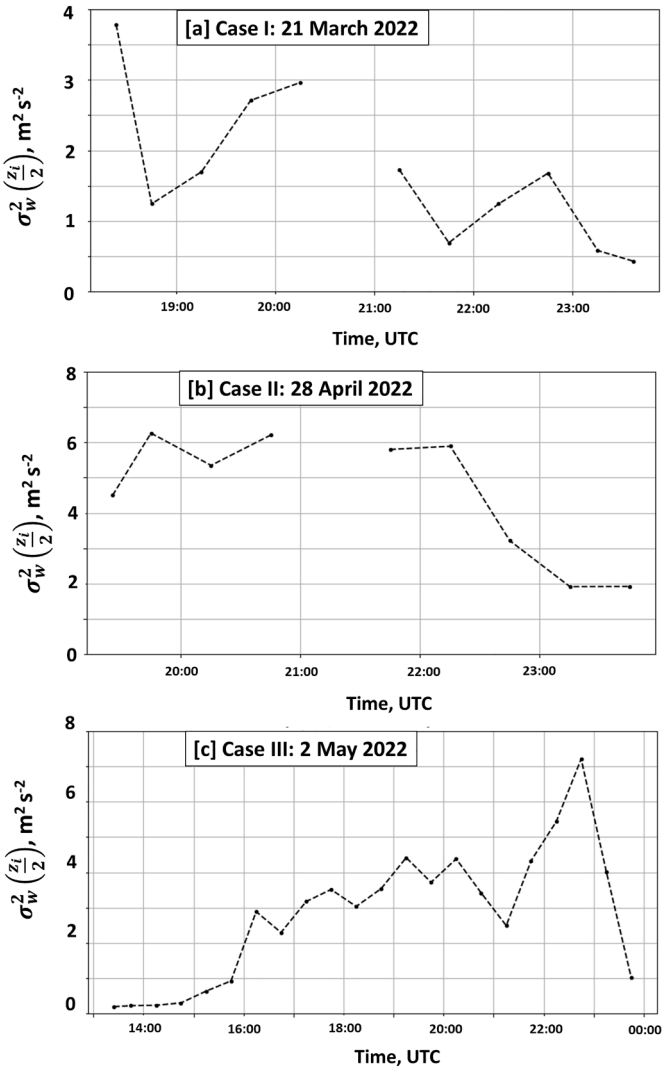

Fig. A.7. Temporal variability in vertical velocity variance observed around $z_i/2$ (i.e., $\sigma_w^2(\frac{z_i}{2})$ in $m^2\ s^{-2}$) during case I (panel a), II (panel b), and III (panel c).

Table A1
Sensor resolution and accuracy for WTM sensors used in this study.

Sensor	Resolution	Accuracy
WTM WS	0.03 ms^{-1}	0.3 ms^{-1}
WTM WD	0.05°	3°
WTM Temperature	0.01 °C	± 0.2 °C
WTM RH	0.1 %	± 3 %

Data availability

The radiosonde datasets used in this study were obtained from the IGRA data archive available at (ftp://ftp.ncdc.noaa.gov/pub/data/igra/data/). The synoptic analyses and associated maps are available from Weather Prediction Center archive (https://www.wpc.ncep.noaa.gov/archives/web_pages/sfc/sfc_archive.php) and the METAR data were obtained from NWS archive (https://www.aviationweather.gov/metar). Lidar data will be made available on request. Additionally, air quality information reports and relevant statistics were freely available directly from the US EPA site (https://www.epa.gov/outdoor-air-quality-data). Doppler lidar data and other meteorological measurements will be made available on request.

References

Achakulwisut, P., Mickley, L.J., Anenberg, S.C., 2018. Drought-sensitivity of fine dust in the US southwest: implications for air quality and public health under future climate change. Environ. Res. Lett. 13 (5). https://doi.org/10.1088/1748-9326/aabf20.

Anand, M., Pal, S., 2022. Exploring atmospheric boundary layer depth variability in frontal environments over an arid region. Bound.-Layer Meteorol. 186. https://doi.org/10.1007/s10546-022-00756-z.

Ashley, W.S., Strader, S., Dziubla, D.C., Haberlie, A., 2015. Driving blind: weather-related vision hazards and fatal motor vehicle crashes. Bull. Amer. Meteor. Soc. 96, 755–778. https://doi.org/10.1175/BAMS-D-14-00026.1.

Barlow, J.F., Dunbar, T.M., Nemitz, E.G., Wood, C.R., Gallagher, M.W., Davies, F., O'Connor, E., Harrison, R.M., 2011. Boundary layer dynamics over London, UK, as

observed using Doppler lidar during REPARTEE-II. Atmos. Chem. Phys. 11, 2111–2125. https://doi.org/10.5194/acp-11-2111-2011.
Beck, H.E., Zimmermann, N.E., McVicar, T., Vergopolan, N., Berg, A., Wood, E.F., 2018. Present and future Köppen-Geiger climate classification maps at 1-km resolution. Sci. Data. 5. https://doi.org/10.1038/sdata.2018.214.
Behrendt, A., Wagner, G., Petrova, A., Shiller, M., Pal, S., Schaberl, T., Wulfmeyer, V., 2005. Modular lidar systems for high-resolution 4-dimensional measurements of water vapor, temperature, and aerosols. In: Proc. SPIE 5653, Lidar Remote Sensing for Industry and Environmental Monitoring V. https://doi.org/10.1117/12.579139.
Behrendt, A., Wulfmeyer, V., Hammann, E., Muppa, S.K., Pal, S., 2015. Profiles of second- to fourth-order moments of turbulent temperature fluctuations in the convective boundary layer: first measurements with rotational Raman lidar. Atmos. Chem. Phys. 15, 5485–5500. https://doi.org/10.5194/acp-15-5485-2015.
Bentley, M.L., Ashley, W.S., Stallins, J.A., 2010. Climatological radar delineation of urban convection for Atlanta, Georgia. Int. J. Climatol. 30, 1589–1594.
Bhowmick, M., Parker, D.J., 2018. Analytical solution to a thermodynamic model for the sensitivity of afternoon deep convective initiation to the surface Bowen ratio. Q. J. Roy. Meteorol. Soc. 144, 2216–2229. https://doi.org/10.1002/qj.3340.
Bluestein, H.B., 2008. Surface boundaries of the southern plains: their role in the initiation of convective storms. Synoptic—dynamic meteorology and weather analysis and forecasting. Meteorol. Monogr. 33 (5). https://doi.org/10.1007/978-0-933876-68-2_1.
Buban, M.S., Ziegler, C.L., Rasmussen, E.N., Richardson, Y.P., 2007. The dryline on 22 May 2002 during IHOP: ground-radar and in situ data analyses of the dryline and boundary layer evolution. Mon. Wea. Rev. 135 (7), 2473–2505. https://doi.org/10.1175/MWR3453.1.
Buban, M.S., Ziegler, C.L., Mansell, E.R., Richardson, Y.P., 2012. Simulation of dryline misovortex dynamics and cumulus formation. Mon. Wea. Rev. 140 (11), 3525–3551.
Burow, D., Ellis, K., 2021. Precipitation and synoptic weather types on hazardous weather days in the southeastern US. Theor. Appl. Climatol. 146, 213–229. https://doi.org/10.1007/s00704-021-03732-8.
Campbell, J.F., Lin, B., Dobler, J., Pal, S., Davis, K., Obland, M.D., et al., 2020. Field evaluation of column CO2 retrievals froms intensity-modulated continuous-wave differential absorption lidar measurements during the ACT-America campaign. Earth and Space Science 7, e2019EA000847. https://doi.org/10.1029/2019EA000847.
Chen, Y.-C., Tseng, W.-L., Wu, C.-M., Chen, W.-T., Chang, C.-H., Tseng, H.-Y., 2023. Influence of synoptic weather on aerosol variability over East Asia: present and future. Atmos. Res. 295, 107023. https://doi.org/10.1016/j.atmosres.2023.107023.
Clark, N.E., 2023. A Lidar-based Investigation of Entrainment Zone Processes Over a Semiarid Region. MS Thesis at Texas Tech University. https://hdl.handle.net/2346/96761.
Clark, N.E., Pal, S., Lee, T.R., 2022. Empirical evidence for the frontal modification of atmospheric boundary layer depth variability over land. J. Appl. Meteorol. https://doi.org/10.1175/JAMC-D-21-0099.1. Climatol, (published online ahead of print 2022).
Conder, M.R.P., 2005. Characteristics of the Quiescent Dryline From a Case Study Perspective. PhD. dissertation. Dept. of Geosciences, Texas Tech University, 211 pp. https://ttu-ir.tdl.org/handle/2346/1135.
Couvreux, F., Rio, C., Guichard, F., Lothon, M., Canut, G., Bouniol, D., Gounou, A., 2011. Initiation of daytime local convection in a semiarid region analysed with high-resolution simulations and AMMA observations. Q.J.R. Meteorol. Soc. 138, 56–71. https://doi.org/10.1002/qj.903.
Davis, K.J., et al., 2021. The atmospheric carbon and transport (ACT)-America Mission. Bull. Amer. Meteor. Soc. 102, E1714–E1734. https://doi.org/10.1175/BAMS-D-20-0300.1.
Dhaliwal, H., Pal, S., Hirth, B., 2023. Unraveling Aerosol – Boundary Layer Interactions in Arid Regions: Insights from Aerosol Optical Thickness measurements over the West Texas Panhandle, 2023 American Geophysical Union Fall Meeting, San Francisco, CA, Dec 2023. https://sites.google.com/view/s3maap/s3-maap-gallery/agu-2023?authuser=0.
Dieudonné, E., Delbarre, H., Augustin, P., Fourmentin, M., Flament, P., Deboudt, K., Cazier, F., 2024. Can commercial Doppler lidars serve air quality applications? Results from a field comparison with PM10, PM2.5, and granulometric observations in a multi-influenced harbor city. Aerosol Science and Technology 1–15. https://doi.org/10.1080/02786826.2024.2427868.
Durre, I., Yin, X., 2008. Enhanced radiosonde data for studies of vertical structure. Bull. Amer. Meteor. Soc. 89 (9), 1257–1262. https://doi.org/10.1175/2008BAMS2603.1.
Durre, I., Vose, R.S., Wuertz, D.B., 2006. Overview of the integrated global radiosonde archive. J. Climate 19, 53–68. https://doi.org/10.1175/JCLI3594.1.
Eck, T.F., Holben, B.N., Kim, J., Beyersdorf, A.J., Choi, M., Lee, S., Park, S., 2020. Influence of cloud, fog, and high relative humidity during pollution transport events in South Korea: aerosol properties and PM2. 5 variability. Atmos. Env. 232, 117530.
EPA, 2021. Climate Change and Social Vulnerability in the United States: A Focus on Six Impacts. U.S. Environmental Protection Agency. EPA 430-R-21-003. www.epa.gov/cira/social-vulnerability-report.
Feng, S., Fu, Q., 2013. Expansion of global drylands under a warming climate. Atmos. Chem. Phys. 13, 10081–10094. https://doi.org/10.5194/acp-13-10081-2013.
Feng, J., Li, Y., Qiu, Y., Zhu, F., 2023. Capturing synoptic-scale variations in surface aerosol pollution using deep learning with meteorological data. Atmos. Chem. Phys. 23, 375–388. https://doi.org/10.5194/acp-23-375-2023.
Findell, K.L., Eltahir, E.A.B., 2003. Atmospheric controls on soil moisture–boundary layer interactions. Part I: framework development. J. Hydrometeor. 4, 552–569. https://doi.org/10.1175/1525-7541(2003)004<0552:ACOSML>2.0.CO;2.
Forster, P., Storelvmo, T., Armour, K., Collins, W., Dufresne, J.-L., Frame, D., Lunt, D.J., Mauritsen, T., Palmer, M.D., Watanabe, M., Wild, M., Zhang, H., 2021. The Earth's energy budget, climate feedbacks, and climate sensitivity. In: Masson-Delmotte, V., Zhai, P., Pirani, A., Connors, S.L., Péan, C., Berger, S., Caud, N., Chen, Y., Goldfarb, L., Gomis, M.I., Huang, M., Leitzell, K., Lonnoy, E., Matthews, J.B.R., Maycock, T.K., Waterfield, T., Yelekçi, O., Yu, R., Zhou, B. (Eds.), Climate Change 2021: The Physical Science Basis. Contribution of Working Group I to the Sixth Assessment Report of the Intergovernmental Panel on Climate Change. Cambridge University Press, Cambridge, United Kingdom and New York, NY, USA, pp. 923–1054. https://doi.org/10.1017/9781009157896.009.
Geerts, B., Damiani, R., Haimov, S., 2006. Finescale vertical structure of a cold front as revealed by an airborne Doppler radar. Mon. Wea. Rev. 134 (1), 251–271. https://doi.org/10.1175/MWR3056.1.
Grini, A., Myhre, G., Zender, C.S., Isaksen, S.A., 2005. Model simulation of dust sources and transport in the global atmosphere: effects of soil erodibility and wind speed variability. J. Geophys. Res. 110, 1–14. https://doi.org/10.1029/2004JD005037.
Han, B., Zhou, T., Zhou, X., Fang, S., Huang, J., He, Q., Huang, Z., Wang, M., 2022. A new algorithm of atmospheric boundary layer height determined from polarization Lidar. Remote Sens. (Basel) 14, 5436. https://doi.org/10.3390/rs14215436.
Hane, C.E., Baldwin, M.E., Bluestein, H.B., Crawford, T.M., Rabin, R.M., 2001. A case study of severe storm development along a dryline within a synoptically active environment. Part I: dryline motion and an eta model forecast. Mon. Wea. Rev. 129, 2183–2204. https://doi.org/10.1175/1520-0493(2001)129<2183:ACSOSS>2.0.CO;2.
Hara, K., Takashima, H., Yoshino, A., Takami, A., Nishita-Hara, C., Fujiyoshi, Y., Hayashi, M., 2022. Seasonal variations of diurnal cycles of aerosols and gases in the Fukuoka plain, Japan: effects of local meteorology and atmospheric chemistry. Atmos. Environ. 289, 119318.
Hoch, J., Markowski, P., 2005. A climatology of springtime dryline position in the U.S. Great Plains Region. J. Climate 18, 2132–2137. https://doi.org/10.1175/JCLI3392.1.
Hogan, R.J., Grant, A.L.M., Illingworth, A.J., Pearson, G.N., O'Connor, E.J., 2009. Vertical velocity variance and skewness in clear and cloud-topped boundary layers as revealed by Doppler Lidar. Q.J.R. Meteorol. Soc. 135, 635–643. https://doi.org/10.1002/qj.413.
Holben, B.N., Kim, J., Sano, I., Mukai, S., Eck, T.F., Giles, D.M., Schafer, J.S., Sinyuk, A., et al., 2018. An overview of mesoscale aerosol processes, comparisons, and validation studies from DRAGON networks. Atmos. Chem. Phys. 18, 655–671. https://doi.org/10.5194/acp-18-655-2018.
Huang, J., Wang, T., Wang, W., Li, Z., Yan, H., 2014. Climate effects of dust aerosols over East Asian arid and semiarid regions. J. Geophys. Res. Atmos. 119, 11398–11416. https://doi.org/10.1002/2014JD021796.
Huang, J., Yu, H., Guan, X., et al., 2016. Accelerated dryland expansion under climate change. Nature. Clim. Change. 6, 166–171. https://doi.org/10.1038/nclimate2837.
Huang, M., Gao, Z., Miao, S., Chen, F., Lemone, M.A., Li, J., Hu, F., Wang, L., 2017a. Estimate of boundary-layer depth over Beijing, China, using Doppler lidar data during SURF-2015. Bound.-Layer Meteor. 162, 503–522. https://doi.org/10.1007/s10546-016-0205-2.
Huang, J., et al., 2017b. Dryland climate change: recent progress and challenges. Rev. Geophys. 55, 719–789. https://doi.org/10.1002/2016RG000550.
Hulme, M., 1996. Recent climatic change in the world's drylands. Geophys. Res. Lett. 23 (1), 61–64. https://doi.org/10.1029/95GL03586.
Jhun, I., Coull, B.A., Schwartz, J., Hubbell, B., Koutrakis, P., 2015. The impact of weather changes on air quality and health in the United States in 1994–2012. Environ. Res. Lett. 10, 84009. https://doi.org/10.1088/1748-9326/10/8/084009.
Kassomenos, P., Kotroni, V., Kallos, G., 1995. Analysis of climatological and air quality observations from Greater Athens Area. Atmos. Environ. 29, 3671–3688. https://doi.org/10.1016/1352-2310(94)00358-r.
Kimmel, T.M., Nielsen-Gammon, J., Rose, B., Mogil, H.M., 2016. The weather and climate of Texas: a big state with big extremes. Weatherwise 69, 25–33. https://doi.org/10.1080/00431672.2016.1206446.
Klingmüller, K., Lelieveld, J., 2023. Data-driven aeolian dust emission scheme for climate modelling evaluated with EMAC 2.55.2. Geosci. Model Dev. 16, 3013–3028. https://doi.org/10.5194/gmd-16-3013-2023.
Kokkalis, P., 2017. Using paraxial approximation to describe the optical setup of a typical EARLINET lidar system. Atmos. Meas. Tech. 10, 3103–3115. https://doi.org/10.5194/amt-10-3103-2017.
Kokkalis, P., Alexiou, D., Papayannis, A., et al., 2020. Application and testing of the extended-Kalman-filtering technique for determining the planetary boundary-layer height over Athens, Greece. Bound.-Lay. Meteorol. 176, 125–147. https://doi.org/10.1007/s10546-020-00514-z.
Koster, R.D., et al., 2004. Regions of strong coupling between soil moisture and precipitation. Science 305, 1138–1140. https://doi.org/10.1126/science.1100217.
Ledari, D.G., Hamidi, M., Shao, Y., 2020. Evaluation of the 13 April 2011 frontal dust storm in west Asia. Aeolian Res. 44, 100592. https://doi.org/10.1016/j.aeolia.2020.100592.
Lee, T.R., Pal, S., 2017. On the potential of 25 years (1991–2015) of rawinsonde measurements for elucidating key climatological and spatiotemporal patterns of afternoon boundary layer depths over the contiguous US. Adv. Meteorol. 19. https://doi.org/10.1155/2017/6841239.
Lee, T.R., Pal, S., Krishnan, P., Hirth, B., Heuer, M., Meyers, T.P., Saylor, R.D., Schroeder, J., 2023. On the efficacy of Monin–Obukhov and Bulk Richardson surface-layer parameterizations over drylands. J. Appl. Meteor. Climatol. 62, 1655–1675. https://doi.org/10.1175/JAMC-D-23-0092.1.
Lenschow, D.H., Stephens, P.L., 1980. The role of thermals in the convective boundary layer. Bound.-Lay. Meteorol. 19, 509–532. https://doi.org/10.1007/BF00122351.
Liu, C., Huang, J., Tao, X., Deng, L., Fang, X., Liu, Y., Luo, L., Zhang, Z., Xiao, H.-W., Xiao, H.-Y., 2021a. An observational study of the boundary-layer entrainment and

impact of aerosol radiative effect under aerosol-polluted conditions. Atmos. Res. https://doi.org/10.1016/j.atmosres.2020.105348.
Liu, S., Xing, J., Sahu, S., Liu, X., Liu, S., Jiang, Y., Zhang, H., Li, S., Ding, D., Chang, X., 2021b. Wind-blown dust and its impacts on particulate matter pollution in Northern China: current and future scenarios. Environ. Res. Lett. 16, 114041.
Lynn, J., Peeva, N., 2021. Communications in the IPCC's sixth assessment report cycle. Clim. Change 169, 18. https://doi.org/10.1007/s10584-021-03233-7.
Ma, M., Pu, Z., Wang, S., Zhang, Q., 2011. Characteristics and numerical simulations of extremely large atmospheric boundary-layer heights over an arid region in Northwest China. Boundary-Layer. Meteorol. 140, 163–176. https://doi.org/10.1007/s10546-011-9608-2.
Ma, Y., Ye, J., Xin, J., Zhang, W., Vilà-Guerau de Arellano, J., Wang, S., Zhao, D., Dai, L., Ma, Y., Wu, X., Xia, X., Tang, G., Wang, Y., Shen, P., Lei, Y., Martin, S.T., 2020. The stove, dome, and umbrella effects of atmospheric aerosol on the development of the planetary boundary layer in hazy regions. Geophys. Res. Lett. 47, e2020GL087373. https://doi.org/10.1029/2020GL087373.
Marsham, J.H., Parker, D.J., Grams, C.M., Johnson, B.T., Grey, W.M.F., Ross, A.N., 2008. Observations of mesoscale and boundary-layer circulation affecting dust uplift and transport in the Saharan boundary-layer. Atmos. Chem. Phy. Discuss. 8, 8817–8845.
McGrath-Spangler, E.L., Denning, A.S., 2013. Global seasonal variations of midday planetary boundary layer depth from CALIPSO space-borne LIDAR. J. Geophys. Res. Atmos. 118, 1226–1233. https://doi.org/10.1002/jgrd.50198.
Mesinger, F., et al., 2006. North American regional reanalysis. Bull. Amer. Meteor. Soc. 87, 343–360. https://doi.org/10.1175/BAMS-87-3-343.
Miller, P.W., Mote, T.L., 2018. Characterizing severe weather potential in synoptically weakly forced thunderstorm environments. Nat. Hazards Earth Syst. Sci. 18, 1261–1277. https://doi.org/10.5194/nhess-18-1261-2018.
Molod, A., Salmun, H., Collow, A.B.M., 2019. Annual cycle of planetary boundary layer heights estimated from wind profiler network data. J. Geophys. Res. Atmos. 124, 6207–6221. https://doi.org/10.1029/2018JD030102.
NASEM (National Academies of Sciences, Engineering, and Medicine), 2018a. The Future of Atmospheric Boundary Layer Observing, Understanding, and Modeling: Proceedings of a Workshop. The National Academies Press, Washington, DC. https://doi.org/10.17226/25138.
NASEM (National Academies of Sciences, Engineering, and Medicine), 2018b. Thriving on Our Changing Planet: A Decadal Strategy for Earth Observation From Space. The National Academies Press, Washington, DC. https://doi.org/10.17226/24938.
NOAA/NWS, 2020. NOWData – NOAA Online Weather Data. National Weather Service Amarillo, TX. Subset used: January 2020-December 2020. https://www.weather.gov/ama/.
NOAA/NWS Midland/Odessa, TX, 2020. Preliminary Monthly Climate Data. National Weather Service Midland/Odessa, TX. https://www.weather.gov/maf/.
Pal, S., Haeffelin, M., 2015. Forcing mechanisms governing diurnal, seasonal, and interannual variability in the boundary layer depths: five years of continuous lidar observations over a suburban site near Paris. J. Geophys. Res. Atmos. 120 (11), 11936–11956. https://doi.org/10.1002/2015JD023268.
Pal, S., Lee, T.R., 2019a. Advected airmass reservoirs in the downwind of mountains and their roles in overrunning boundary layer depths over the plains. Geophys. Res. Lett. 46. https://doi.org/10.1029/2019GL083988.
Pal, S., Lee, T.R., 2019b. Contrasting air mass advection explains significant differences in boundary layer depth seasonal cycles under onshore versus offshore flows. Geophys. Res. Lett. 46. https://doi.org/10.1029/2018GL081699.
Pal, S., Behrendt, A., Bauer, H., Radlach, M., Riede, A., Schiller, M., Wagner, G., Wulfmeyer, V., 2008. 3-Dimensional observations of atmospheric variables during the field campaign COPS IOP. Earth and Environmental Sciences 1, 012031. https://doi.org/10.1088/1755-1307/1/1/012031.
Pal, S., Behrendt, A., Wulfmeyer, V., 2010. Elastic-backscatter-lidar-based characterization of the convective boundary layer and investigation of related statistics. Ann. Geophys. 28, 825–847.
Pal, S., Haeffelin, M., Batchvarova, E., 2013. Exploring a geophysical process-based attribution technique for the determination of the atmospheric boundary layer depth using aerosol lidar and near-surface meteorological measurements. J. Geophys. Res. Atmos. 118, 9277–9295. https://doi.org/10.1002/jgrd.50710.
Pal, S., Lee, T.R., Phelps, S., De Wekker, S.F.J., 2014. Impact of atmospheric boundary layer depth variability and wind reversal on the diurnal variability of aerosol concentration at a valley site. Sci. Total Environ. https://doi.org/10.1016/j.scitotenv.2014.07.067.
Pal, S., Davis, K.J., Lauvaux, T., Browell, E.V., Gaudet, B.J., Stauffer, D.R., Obland, M.D., Choi, Y., DiGangi, J.P., Feng, S., Lin, B., Miles, N.L., Pauly, R.M., Richardson, S.J., Zhang, F., 2020. Observations of greenhouse gas changes across summer frontal boundaries in the eastern United States. J. Geophys. Res.-Atmos. 125, e2019JD030526. https://doi.org/10.1029/2019JD030526.
Pal, S., Clark, N.E., Lee, T.R., Conder, M., Buban, M., 2021. When and where horizontal advection is critical to alter atmospheric boundary layer dynamics over land: the need for a conceptual framework. Atmos. Res. 264. https://doi.org/10.1016/j.atmosres.2021.105825.
Peckham, S.E., Wilhelmson, R.B., Wicker, L.J., Ziegler, C.L., 2004. Numerical simulation of the interaction between the dryline and horizontal convective rolls. Mon. Weather Rev. 132, 1792–1812. https://doi.org/10.1175/1520-0493(2004)132%3C1792:NSOTIB%3E2.0.CO;2.
Peter, J.R., Siems, S.T., Jensen, J.B., Gras, J.L., Ishizaka, Y., Hacker, J.M., 2010. Airborne observations of the effect of a cold front on the aerosol particle size distribution and new particle formation. Q.J.R. Meteorol. Soc. 136, 944–961. https://doi.org/10.1002/qj.515.
Pietersen, H.P., Vilà-Guerau de Arellano, J., Augustin, P., van de Boer, A., de Coster, O., Delbarre, H., Durand, P., Fourmentin, M., Gioli, B., Hartogensis, O., Lohou, F., Lothon, M., Ouwersloot, H.G., Pino, D., Reuder, J., 2015. Study of a prototypical convective boundary layer observed during BLLAST: contributions by large-scale forcings. Atmos. Chem. Phys. 15, 4241–4257.
Pozo, D., Marín, J.C., Raga, G.B., Arévalo, J., Baumgardner, D., Córdova, A.M., Mora, J., 2019. Synoptic and local circulations associated with events of high particulate pollution in Valparaiso, Chile. Atmos. Env. 96, 164–178. https://doi.org/10.1016/j.atmosenv.2018.10.006.
Reinman, S.L., 2013. Intergovernmental panel on climate change (IPCC). Encycl. Energy Nat. Resour. Environ. Econ. 26, 48–56.
Safriel, U., et al., 2005. Dryland systems. In: Hassan, R., Scholes, R., Ash, N. (Eds.), Ecosystems and Human Wellbeing, Current State and Trends. Island Press, Washington, D. C, pp. 623–662.
Scaff, L., Prein, A.F., Li, Y., et al., 2021. Dryline characteristics in North America's historical and future climates. Climate Dynam. 57, 2171–2188. https://doi.org/10.1007/s00382-021-05800-1.
Schroeder, J.L., Burgett, W.S., Haynie, K.B., Sonmez, I., Skwira, G.D., Doggett, A.L., Lipe, J.W., 2005. The West Texas Mesonet: a technical overview. J. Atmos. Oceanic Tech. 22 (2), 211–222.
Schultz, D.M., 2004. Cold fronts with and without prefrontal wind shifts in the Central United States. Mon. Wea. Rev. 132 (8), 2040–2053. https://doi.org/10.1175/1520-0493(2004)132<2040:CFWAWP>2.0.CO;2.
Sheih, C.M., Johnson, S.A., DePaul, F.T., 1983. Case studies of aerosol size distribution and chemistry during passages of a cold and a warm front. Atmospheric Environ. 17 (7), 1299–1306. https://doi.org/10.1016/0004-6981(83)90404-3.
Sinclair, V., 2013. A 6-year climatology of fronts affecting Helsinki, Finland, and their boundary layer structure. J Appl Meteor Climatol 52 (9), 2106–2124.
Soil Survey Staff, Natural Resources Conservation Service, United States Department of Agriculture, 2023. Web Soil Survey. http://websoilsurvey.nrcs.usda.gov/.
Sorooshian, A., Wonaschütz, A., Jarjour, E.G., Hashimoto, B.I., Schichtel, B.A., Betterton, E.A., 2011. An aerosol climatology for a rapidly growing arid region (southern Arizona): major aerosol species and remotely sensed aerosol properties. J. Geophys. Res. 116, D19205. https://doi.org/10.1029/2011JD016197.
Stull, R.B., 1988. An Introduction to Boundary Layer Meteorology, 666 pp.. Kluwer Academic Publishers, Dordrecht, Netherlands. https://doi.org/10.1007/978-94-009-3027-8.
Takashima, H., Hara, K., Nishita-Hara, C., Fujiyoshi, Y., Shiraishi, K., Hayashi, M., Yoshino, A., Takami, A., Yamazaki, A., 2019. Short-term variation in atmospheric constituents associated with local front passage observed by a 3-D coherent Doppler lidar and in-situ aerosol/gas measurements. Atmos. Environ. X 3, 100043. https://doi.org/10.1016/j.aeaoa.2019.100043.
Takemi, T., 1999. Structure and evolution of a severe squall line over the arid region in northwest China. Mon. Wea. Rev. 127, 1301–1309. https://doi.org/10.1175/1520-0493(1999)127<1301:SAEOAS>2.0.CO;2.
Taylor, C.M., Parker, D.J., Lloyd, C.R., Thorncroft, C.D., 2005. Observations of synoptic-scale land surface variability and its coupling with the atmosphere. Q.J.R. Meteorol. Soc. 131, 913–937. https://doi.org/10.1256/qj.04.119.
Teixeira, J., et al., 2021. Toward a Global Planetary Boundary Layer Observing System: The NASA PBL Incubation Study Team Report. NASA PBL Incubation Study Team, p. 134.
Tong, D., Feng, I., Gill, T.E., Schepanski, K., Wang, J., 2023. How many people were killed by windblown dust events in the United States? Bull. Amer. Meteor. Soc. 104, E1067–E1084. https://doi.org/10.1175/BAMS-D-22-0186.1.
Tucker, S.C., Senff, C.J., Weickmann, A.M., Brewer, W.A., Banta, R.M., Sandberg, S.P., Law, D.C., Hardesty, R.M., 2009. Doppler Lidar estimation of mixing height using turbulence, shear, and aerosol profiles. J. Atmos. Oceanic Tech. 26, 673–688. https://doi.org/10.1175/2008JTECHA1157.1.
Vakkari, V., Baars, H., Bohlmann, S., Bühl, J., Komppula, M., Mamouri, R.E., O'Connor, E.J., 2021. Aerosol particle depolarization ratio at 1565 nm measured with a Halo Doppler lidar. Atmos. Chem. Phys. 21 (8), 5807–5820. https://doi.org/10.5194/acp-21-5807-2021.
van Schalkwyk, L., Blamey, R.C., Dyson, L.L., Reason, C.J.C., 2022. A climatology of drylines in the interior of subtropical Southern Africa. J. Climate 35, 6411–6430. https://doi.org/10.1175/JCLI-D-21-1005.1.
Vega, A.R., Antuña-Marrero, J.C., Barriopedro, D., García-Herrera, R., Cachorro Revilla, V.E., Frutos Baraja, A., Antuña-Sánchez, J.C., 2022. Climatology of aerosols over the Caribbean Islands: aerosol types, synoptic patterns, and transport. J. Appl. Meteorol. Clim. https://doi.org/10.1175/JAMC-D-21-0015.1.
Walley, S., Pal, S., Campbell, J.F., Dobler, J., Bell, E., Weir, B., et al., 2022. Airborne lidar measurements of XCO2 in synoptically active environment and associated comparisons with numerical simulations. J. Geophys. Res. Atmos. 127, e2021JD035664. https://doi.org/10.1029/2021JD035664.
Wehbe, Y., Temimi, M., Weston, M., Chaouch, N., Branch, O., Schwitalla, T., Wulfmeyer, V., Zhan, X., Liu, J., Al Mandous, A., 2019. Analysis of an extreme weather event in a hyper-arid region using WRF-hydro coupling, station, and

satellite data. Nat. Hazards Earth Syst. Sci. 19, 1129–1149. https://doi.org/10.5194/nhess-19-1129-2019.

Wulfmeyer, V., Pal, S., Turner, D.D., et al., 2010. Can water vapour Raman Lidar resolve profiles of turbulent variables in the convective boundary layer? Boundary-Layer Meteorol 136, 253–284. https://doi.org/10.1007/s10546-010-9494-z.

Wulfmeyer, V., et al., 2018. A new research approach for observing and characterizing land-atmosphere feedback. Bull.Amer. Meteor.Soc. 99, 1639–1667. https://doi.org/10.1175/BAMS-D-17-0009.1.

Xue, M., Martin, W.J., 2006. A high-resolution modeling study of the 24 May 2002 dryline case during IHOP. Part II: horizontal convective rolls and convective initiation. Mon. Weather Rev. 134, 172–191. https://doi.org/10.1175/MWR3072.1.

Yun, Y., Gao, R., Yue, H., Guo, L., Li, G., Sang, N., 2017. Sulfate aerosols promote lung cancer metastasis by epigenetically regulating the epithelial-to-mesenchymal transition (EMT). Environ. Sci. Technol. 51 (19), 11401–11411. https://doi.org/10.1021/acs.est.7b02857.

Zhang, Q., et al., 2005. NWC-ALIEX and its research advances (in Chinese). Adv. Earth Sci. 20, 427–441.

Zhang, Q., Ma, X., Tie, X., Huang, M., Zhao, C., 2009. Vertical distributions of aerosols under different weather conditions: analysis of in-situ aircraft measurements in Beijing, China. Atmos. Env. 43 (34), 5526–5535.